Marshall Plan Scholarship

Report

Peter Wagner
University of Leoben in cooperation with
University of North Texas and
Los Alamos National Laboratory

A study on the Behavior of Interstitial Elements in Nickel Super-alloys

The overall aim of this work is to understand diffusion and distribution of interstitial and alloying additions in Ni_3Al by coupling ab initio calculation and experiments. The results obtained from the Vienna Ab Initio Simulation Package (VASP) were compared with the data from high temperature carburization and high temperature oxidation experiments. The samples were characterized using optical microscopy, Scanning electron microscope, Focused Ion Beam microscope, Energy dispersive X-ray spectroscopy, and other techniques. This enabled us to develop insights into the high temperature corrosion experimental results such as shown in this thesis. This will lead to a better understanding of the mechanisms of high-temperature corrosion in Ni-based super alloys.

INDEX

1. Behavior of interstitial elements in Nickel-Based Super Alloys

Gas turbines used in jet engines and gas-fired land-based turbines for electricity generation are the most advanced energy conversion devices in use. A single unit of the latter can produce about 480 MW. A typical inlet temperature in a gas turbine engine exceeds 1650 K [1]. Furthermore, the thermodynamic efficiency of an engine is directly related to its operation temperature. Handling such large temperatures are challenging for the materials used for turbine blades. In addition to high strengths, turbine blade materials must exhibit good creep and oxidation resistance. Many iron, cobalt, and nickel based super alloys have been developed for use under extreme conditions.

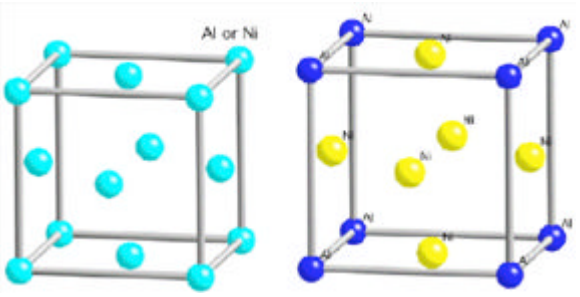

Figure 1: (a) face-centered-cubic (FCC) crystal structure of γ. (b) FCC crystal structure of γ'. [1]

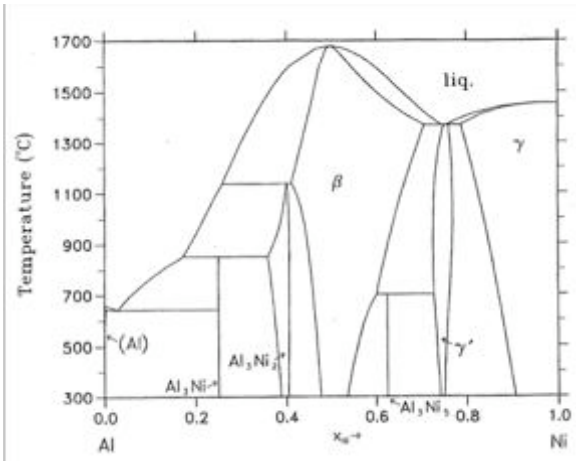

Figure 2: Calculated Ni-Al Phase Diagram [2]

Nickel based super alloys are preferred for jet engine applications. The essential solutes in nickel based super alloys are aluminium and/or titanium, with a total concentration which is typically less than 10 atomic percent. This generates a two-phase equilibrium microstructure consisting of random distribution of Al in Ni (NiAl gamma, γ) and ordered Ni_3Al (gamma-prime, γ') shown in Figure 1. The γ' precipitate phase is largely responsible for the elevated-temperature strength of the material and its incredible resistance to creep deformation. The amount of γ' depends on the chemical composition and temperature, as illustrated in the binary phase diagram in Figure 2.

The Ni-Al binary phase diagram show the γ and γ' phase field. For a given chemical composition, the fraction of γ ' decreases as the temperature is increased. This behaviour is used to dissolve γ' at a sufficiently high temperature (a solution treatment) followed by ageing at a lower temperature to generate a uniform and fine dispersion of these strengthening precipitates. However, as can be seen from the (γ + γ')/ γ' phase boundary on the isothermal ternary sections of the Ni, Al phase diagram, the γ' phase is not strictly stoichiometric. An excess of vacancies on one of the sub lattices may lead to deviations from stoichiometry. Alternatively, some of the nickel atoms might occupy the Al sites and vice-versa. In addition to aluminium and titanium, niobium, hafnium and tantalum partition preferentially into γ'.

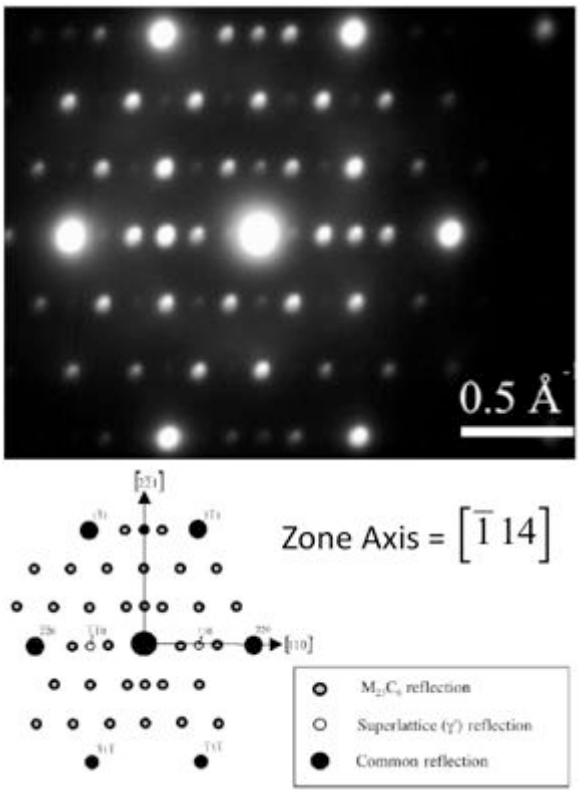

Figure 3: Superimposed electron diffraction pattern from γ, γ ', and $M_{23}C_6$ carbide. The γ and γ ' phases have their cubic-lattice edges perfectly aligned. [3]

The small misfit between the γ and γ' lattices is important for two reasons. Firstly, when combined with the cube-cube orientation relationship, it ensures a low γ / γ' interfacial energy. The ordinary mechanism of precipitate coarsening is driven entirely by the minimization of total interfacial free energy. A coherent or semi-coherent interface therefore makes the microstructure more stable at elevated temperatures.

The magnitude and sign of the misfit also influences the development of microstructure at elevated temperatures. The misfit is said to be positive when the γ' has a larger lattice parameter than γ. The misfit can be controlled by altering the chemical composition, particularly the aluminium or titanium ratio. A negative misfit stimulates the formation of rafts of γ', essentially layers of the phase in a direction normal to the applied stress. This can help reduce the creep rate if the mechanism involves the movement of dislocations across the precipitate rafts.

Commercial super alloys contain more than just Ni, Al and Ti. Chromium and aluminium are essential for oxidation resistance and small quantities of yttrium help the oxide scale to cohere to the substrate. Polycrystalline super alloys contain grain boundary strengthening elements such as boron and zirconium, which segregate to the boundaries. The resulting reduction in grain boundary energy is associated with better creep strength and ductility when the mechanism of failure involves grain decohesion.

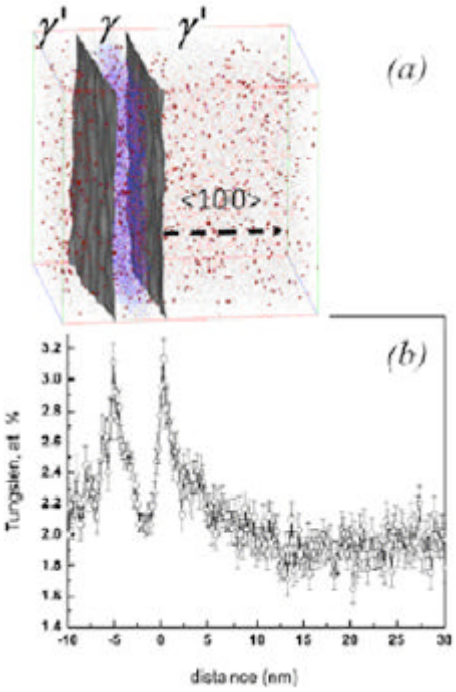

Figure 4: (a) Two 10 at.% Cr Isoconcetration surfaces separating the γ and γ' phases. (b) A proxigram plotted with reference to these isoconcentration surfaces indicate confined segregation of W at both {100} type {100} type γ'/γ interfaces. In addition to the Cr and Al atoms indicated, 50% of the detected W atoms are shown and represented as spheres. [4]

There are also the carbide formers (C, Cr, Mo, W, Nb, Ta, Ti and Hf). The carbides tend to precipitate at grain boundaries and hence reduce the tendency for grain boundary sliding. Elements such as cobalt, iron, chromium, niobium, tantalum, molybdenum, tungsten, vanadium, titanium and aluminium are also solid-solution strengtheners, both in γ and γ'. The electron diffraction patterns from these phases are shown in Figure 4. There are, naturally, limits to the concentrations that can be added without inducing precipitation. It is particularly important to avoid certain embrittling phases such as Laves and Sigma. There are no simple rules governing the critical concentrations. The influence of interstitial elements (C, Cl, N, O), which do occur during normal operation conditions, while burning gas, must also be taken into account. While several damage possibilities caused by those elements are know (carburization, embrittling of grain boundaries) their diffusion behaviour toward the alloying materials is not.

2. Theory

2.1 Theory of Vienna Ab Initio Simulation

Hohenberg and Kohn [5] and Kohn and Sham [6] introduced in 1960 a theory, which predict the total energy of a system such as a solid or a molecule depending only on the electron density of its ground state. Therefore it is possible to express the total energy of an atomistic system as a function of its electron density

$$E = E[\rho] \tag{1}$$

In solid-state systems, molecules and atoms, the electron density is a scalar function defined at each point **r** in real space.

$$\rho = \rho(r) \tag{2}$$

The electron density and the total energy depend on the type and arrangements of the atomic nuclei. Therefore, one can write

$$E = E[\rho(r), \{R_\alpha\}] \tag{3}$$

The set $\{\mathbf{R}_\alpha\}$ denotes the positions of all atoms, α in the system under consideration. Eq. (3) is the key to the atomic-scale understanding of electronic, structural and dynamic properties of matter. Therefore it is possible to predict for example the equilibrium structure of a solid material and the reconstruction of surfaces.

Furthermore, the derivative of the total energy of Eq. 3 with respect to the nuclear position of an atom gives the force acting on that atom, which enables the efficient search for stable structures and the study of dynamical processes such as diffusion or the reaction of molecules on surfaces. The theories and work, which are used today, are mostly based on the Born-Oppenheimer approximation, which assumes that the motions of the electrons are infinitely faster than those of the nuclei. This means that the electronic structure is calculated for a fixed atomic arrangement and the atoms are then moved according to classical

mechanics. For heavy atoms like W this might be good approximation, but may cause errors for light atoms such as H or Li.

In density functional theory, the total energy (Eq. 1) is structured in three parts, a kinetic energy, electrostatic or Coulomb energy and so-called exchange correlation energy,

$$E = T_0 + U + E_{XC} \tag{4}$$

Coulomb energy U, is purely classical and contains the electrostatic energy, which raises from the Coulomb attraction between electrons and nuclei, the repulsion between all electronic charges and the repulsion between nuclei

$$U = U_{en} + U_{ee} + U_{nn} \tag{5}$$

with

$$U_{en} = -e^2 \sum_{\alpha} Z_{\alpha} \int \frac{\rho(r)}{|r - R_{\alpha}|} dr \tag{6}$$

$$U_{ee} = e^2 \iint \frac{\rho(r)\rho(r')}{|r - r'|} dr dr' \tag{7}$$

$$U_{nn} = -e^2 \sum_{\alpha\alpha'} \frac{Z_{\alpha} Z'_{\alpha}}{|R_{\alpha} - R'_{\alpha}|} \tag{8}$$

e is the elementary charge of a proton and Z_α is the atomic number of atom α. The summations extend over all atoms and the integrations over all space. Once the electron density and the atomic numbers and positions of all atoms are known, expression Eq. (6)-(8) can be calculated by classical electrostatic techniques.

The kinetic energy term, T_0, is more difficult to define. In density functional theory (DFT), the “real” electrons of a system are replaced by “effective” electrons with the same charge, mass and density distribution. Effective electrons move as independent particles in an effective potential, whereas the motion of a real electron is correlated with those of all other electrons. T_0 is the sum of the kinetic energies of all effective electrons moving as independent

particles. Often, one does not explicitly make this distinction between real and effective electrons.

If each effective electron is described by a single particle wave function Ψ_i, then the kinetic energy of all effective electrons in the system is given by

$$T_0 = \sum_i n_i \int \Psi_i^*(r)\left[-\frac{\hbar^2}{2m}\nabla^2\right]\Psi_i(r)dr \qquad (9)$$

Eq. 9 is the sum of the expectation values of one-particle kinetic energies; n_i denotes the number of electrons in state i. By construction, dynamic correlations between the electrons are excluded from T_0.

The third term of Eq. 4, called exchange-correlation energy, E_{XC}, includes all remaining electronic contributions to the total energy. The most important of these contributions is the exchange term. Electrons are Fermions and obey the Pauli exclusion principle. In real space, the Pauli principle implies that, around each electron with a given spin, all other electrons with the same spin avoid that electron. Therefore, the average Coulomb repulsion action on the electron is reduced. This energy gain is called exchange energy. Effectively each electron is surrounded by a positive exchange hole. By definition, the additional multiple component interaction terms between electrons of opposite spin are called correlation energy.

As an illustration, the total energy of a single C atom is approximately -1019eV, that of a Si atom E=7859eV and that of a W atom E=-439634 eV [7]. The kinetic energy and the Coulomb energy terms are of similar magnitude but of opposite sign whereas the exchange-correlation term is about 10% of the Coulomb term and attractive for electrons (because the exchange-hole position is positive). The correlation energy is smaller than the exchange energy, but plays an important role in determining the details in the length and strength of interatomic bonds. In fact compared with the total energy, the binding energy of an atom in a solid or a surface is quite small and lies in the range of about 1 to 8 eV. Energies involved in changes of the positions of atoms, such as in the reconstruction of a surface can be even smaller. For example, only about 0.03 eV are required to flip an asymmetric Si-dimer on a reconstructed Si (001) surface from one conformation into another where the role of the upper and lower Si atoms is reversed.

The Hohenberg-Kohn-Sham theorem, which is a central part of the density functional theory, states that the total energy is at its minimum value for the ground state density and that the total energy is stationary with respect to first-order variations in the density,

$$\left.\frac{\partial E[\rho]}{\partial \rho}\right|_{\rho=\rho_0} = 0 \tag{10}$$

In conjunction with the kinetic energy, one-particle wave functions $\Psi_i(\mathbf{r})$, which generate the electron density, were

$$\rho(r) = \sum_i n_i \left|\Psi_i(r)\right|^2 \tag{11}$$

As in the Eq. 9 for the kinetic energy, n_i is the occupation number of the Eigen state I, which is represented by the one-particle wave function Ψ_i. So far, no approximations have been made to the many-electron interactions. By construction, $\rho(\mathbf{r})$ in Eq. 11 is the exact multiple-electron density.

Eq. 10 and 11 introduced one-particle wave functions. A change of these wave functions corresponds to a variation in the electron density. Therefore, the variational condition (Eq.10) can be used to derive the conditions for the one-particle wave functions that lead to the ground state density. To this end, one substitutes Eq.11 in Eq.11 and varies the total energy with respect to each wave function, which leads to the following equations:

$$\left[-\frac{\hbar^2}{2m}\nabla^2 + V_{eff}(r)\right]\Psi_{i(r)} = \in_i \psi_i(r) \tag{12}$$

with

$$V_{eff}(r) = V_C(r) + \mu_{XC}\left[\rho(r)\right] \tag{13}$$

Equations (1-12) are called the Kohn-Sham equations. The electron density, which corresponds to these wave functions, is the ground state density function, which minimizes the total energy. The solutions of the Kohn-Sham equations from an orthonormal set,

$$\int \Psi_i^*(r)\Psi_j(r)dr = \delta_{ij} \tag{14}$$

This additional constraint is achieved by introducing Lagrange multipliers (e_i) in Eq.12. These “Lagrange Multipliers” are effective one-electron Eigen values. These are used to determine the occupation numbers n_i by applying the Aufbau principle. The Eigen states are ordered according to increasing Eigen values. For non-spin polarized systems each state is occupied by at most one electron.

As a consequence of the partitioning of the total energy (Equ.4), the Hamilton operator in the Kohn-Sham equations (Equ.12) contains three terms, one for the kinetic energy, the second for the Coulomb potential and the third for the exchange-correlation potential.

The kinetic energy term is the standard second-order differential operator of one-particle Schrödinger equations and its construction does not require specific knowledge of a system. In contrast, the Coulomb potential operator, $V_C(\mathbf{r})$, and the exchange-correlation potential operator, μ_{XC}, depend on the specific electron distribution in the system.

The Coulomb or electrostatic potential $V_C(\mathbf{r})$ at point **r** is generated from the electric charges off all nuclei and electrons in the system. It can be evaluated directly in real space,

$$V_{C(r)} = -e^2 \sum_{\alpha} \frac{Z_\alpha}{|r - R_\alpha|} + e^2 \int \frac{\rho(r')}{|r - r'|} dr' \qquad (15)$$

In condensed systems it is more convenient to use Poisson’s equation

$$\nabla^2 V_c(r) = -4\pi e^2 q(r) \qquad (16)$$

to calculate the electrostatic potential. Here q(**r**) denotes both the electronic charge distribution ρ(**r**) and the positive point charges of the nuclei at the position $\mathbf{R}_\alpha$.
The exchange-correlation potential is related to the exchange-correlation energy by

$$\mu_{XC} = \frac{\partial E_{XC}[\rho]}{\partial \rho} \qquad (17)$$

Equation 17 is formally exact in the sense that it does not contain any approximations to be the complete many-body interactions. The exchange-correlation energy (and also the exchange-correlation potential) is not known and approximations have to be done.

The exchange-correlation energy depends only on the electron density. As a simple and good approximation one can assume that the exchange-correlation energy depends only on

the local density around each volume element *d***r**. This is called the local density approximation (LDA).

$$E_{XC}[\rho] = \int \rho(r) \in_{EX}^{0} [\rho(r)] dr \qquad (18)$$

In any atomic arrangement such as a crystal, a surface or a molecule, there is a certain electron density ρ(**r**) at each point **r** in space. The LDA then resets on two basic assumptions:

(i) the exchange and correlation effects come predominantly from immediate vicinity of the point **r** and

(ii) these exchange and correlation effects do not depend strongly on the variations of the electron density in the vicinity of **r**.

If conditions (i) and (ii) are reasonably well fulfilled, then the contribution from volume element *d***r** would be the same as if this volume element were surrounded by a constant electron density of the same value as within *d***r**. This is a very close approximation for metallic systems.

A system of interacting electrons with a constant density is called a homogeneous electron gas. Substantial theoretical efforts have been made to understand and characterize such an idealized system. For practical calculations, $\in_{EX} [\rho]$ is expressed as an analytical function of the electron density. There are various analytical forms with different coefficients in their representation of the exchange-correlation terms. These coefficients are not adjustable parameters, but rather they are determined through first principles theory. Hence, the LDA is a first-principles approach in the sense that the quantum mechanical problem is solved without any adjustable, arbitrary or system depended parameters.

	Energy	Potential	
Exchange	$\in_{XC}=\in_X+\in_C$	$\mu=\frac{\partial(\rho\in)}{\partial\rho}$	(19) (20)
Correlation	$\in_X=-\frac{3}{2}\left(\frac{3}{\pi}\rho\right)^{\frac{1}{3}}$	$\mu_X=-2\left(\frac{3}{\pi}\rho\right)^{\frac{1}{3}}$	(21) (22)
	$\in_C=-c\left[\left(1+x^3\right)\ln\left(1+\frac{1}{x}\right)+\frac{x}{2}-x^3-\frac{1}{3}\right]$	$\mu_C=-c\ln\left(1+\frac{1}{x}\right)$	(23) (24)
	$c=0.0225,\quad x=\frac{r_s}{21},\quad r_s=\left(\frac{3}{4\pi\rho}\right)^{\frac{1}{3}}$		(25)

Exchange and correlation energies per electron are denoted by $\in$ and the corresponding potentials by μ. Both quantities are given in Hartree atomic units (1Hartree = 2 Rydberg = 27.21165 eV). The units for the electron density are number of electrons/(Bohrradius)^3.

Note that there are two types of exchange-correlation terms, one for the energy and one for the potential. The energy, $\in_{XC}$, is needed to evaluate the total energy and the potential, μ_{XC}, is required for the Kohn-Sham equations. The two terms are following equations (17) and (18), related.

$$\mu_{XC}=\frac{\partial\left[\rho\in_{XC}(\rho)\right]}{\partial\rho} \qquad (26)$$

Using the explicit formulas given in the table above, one can evaluate the exchange-correlation potential for any electron density ρ(**r**). Thus, all terms of the effective one-particle operator in the Kohn-Sham equations are defined and one can proceed with a computational implementation.

2.1.1 One - Particle Energies

The fundamental quantities in density functional theory are the electron density and the corresponding total energy, but not the one-particle Eigen values. However, the one-electron picture is so useful that one seeks to exploit the Kohn-Sham Eigen value and one-particle wave functions as much as possible. The one-particle energies of effective electrons have been introduced in the derivation of the Kohn-Sham equations as Lagrange multipliers. The Kohn-Sham equations have the form of an Eigen value problem in which each wave function has an associated Eigen values $\in_i$ with an occupation number of n_i. Janak's theorem [8] provides a relationship between the total energy and these Eigen values.

$$\in_i = \frac{\partial E}{\partial n_i} \tag{27}$$

The Eigen value $\in_i$ equals the change of the total energy with the change of the occupation number of level i.

The highest occupied electronic level in a metallic system is called the Fermi energy or the Fermi level, E_F. The nature of the electronic states at E_F play a crucial role in determining materials properties such as electrical conductivity, magnetism and superconductivity. On surface, the energy difference between E_F and the electrostatic potential in the vacuum region, V_0, above the surface is the work function, ϕ. While in general the Kohn-Sham Eigen values are not excitation energies, it was show by Schulte in 1977 [9] that for a metallic system the highest occupied Kohn-Sham Eigen value can be directly interpreted as the work function. Thus, the agreement between experimental and calculated work functions provides a good test for the quality of actual calculations. With present LDA approaches, the calculated values are typically within 0.1-0.2 eV of the experimental results.

2.1.2 Spin - Polarization

So far the discussion of density functional theory was restricted to non-spin-polarized cases. However, many systems such as magnetic transition metals or molecules such as O_2 involve unpaired electrons or molecular radicals and thus require a spin-polarized method. In such systems the number of electrons with “spin-up” can be different from that with “spin-down”. In the early 1970’s von Barth and Hedin [10] and Gunnarson et al. [11] generalized density functional theory with the local spin density
(LSD) approximation.

In the local spin density functional (LSDF) theory, the fundamental quantities are both, the electron density, ρ(**r**) and the spin density, σ(**r**). The spin density is defined as the difference between the density of spin-up electrons and the density of spin-down electrons

$$\sigma(r) = \rho_{\uparrow}(r) - \rho_{\downarrow}(r) \tag{28}$$

with the total electron density

$$\rho(r) = \rho_{\uparrow}(r) - \rho_{\downarrow}(r) \tag{29}$$

In LSDF theory, the exchange-correlation potential for spin-up electrons is in general different form than for spin-down electrons. Consequently, the effective potential (13) becomes dependent on the spin. Thus, the Kohn-Sham equations (12) in their spin-polarized form are

$$\left[-\frac{\hbar^2}{2m}\nabla^2 + V_{eff}^{\sigma}\left(\in_i^{\sigma}\right)\right]\Psi_i^{\sigma}(r), \quad \sigma = \uparrow or \downarrow \tag{30}$$

with

$$V_{eff}^{\sigma}(r) = V_C + \mu_{XC}^{\sigma}\left[\rho(r),\sigma(r)\right] \tag{31}$$

The exchange-correlation potential in LSDF theory depends on both the electron density and the spin density, as written in Eq.24. There are two sets of single-particle wave functions,

one for spin-up electrons and one for spin-down electrons, each with their corresponding one-electron Eigen values. For the case of spin-up and spin-down densities, the spin density is zero throughout space and LSDF theory becomes identical with the LDF approach. Notice that in spin-polarized calculations, the occupation of single-particle states is 1 or 0, but there is only one Fermi energy. In magnetic systems, the spin-up and spin-down electrons are often referred to as “majority” and “minority” spin systems. The table in the next section gives an example of the local spin density exchange-correlation formula by Barth and Hedin.

2.1.3 Generalized Gradient Approximation

A large number of total energy calculations have shown that the LDA gives interatomic bond lengths within ±0.05 Å of experiment or better for a great variety of solids, surfaces and molecules. However the following systematic trends are found:

(iii) most lattice parameters predicted with LDA are too short
(iv) weak bonds are noticeably too short
(v) the binding energies calculated with the LDA are typically too large, sometimes as much as 50% in strongly bound systems and even more in weakly bound materials.

Gradient-corrected density functions offer a remedy. The basic idea in these schemes is the inclusion of terms in the exchange-correlation expression that depend on the gradient of the electron density and not only on its value at each point in space. Therefore, these corrections are also referred to as “non-local” potentials [12,13].

Gradient-correction to the total energy for exchange by Becke and correlation by Perdew

$$E_{GGA} = E_{LSD} + E_X^G + E_C^G \tag{32}$$

Becke (1988):
Gradient-corrected exchange

$$E_X^G = b\sum\int \frac{\rho_\sigma x_\sigma^2}{1+6bx_\sigma \sinh^{-1} x_\sigma} dr \tag{33}$$

$$x_\sigma = \frac{|\nabla\rho|}{\rho^{\frac{4}{3}}} \quad \sigma = \uparrow or \downarrow \tag{34}$$

Perdew (1986):
Gradient-corrected correlation

$$E_C^G = \int f\left(\rho_\uparrow, \rho_\downarrow\right) e^{-g(\rho)|\nabla\rho|} |\nabla\rho|^2 dr \tag{35}$$

Energies and potentials are given in Hartree atomic units; the units for the electron and spin densities are number of electrons/(Bohr radius)^3. The constant b in Becke's formula is a parameter fitted to the exchange energy of inert gases.

2.1.4 Relativistic Effects

Electrons near an atomic nucleus achieve such high kinetic energies that relativistic effects become noticeable even for light atoms at the beginning of the periodic table. For elements with an atomic number above about 54 (Xe) these relativistic effects become quite important and should be included in electronic structure calculations. The relativistic mass enhancements of nuclei lead to a contraction of the electronic charge distribution around the nuclei compared with a non-relativistic treatment. Therefore atoms with about Z>54 non-relativistic calculations can overestimate bond lengths by 0.1 Å and more. Furthermore, relativistic effects change the relative energy of s, p, d and f-states, which can have a significant impact on bonding mechanisms and energies.

Relativistic effects lead to a spin-orbit splitting which is, for example, about 0.3 eV for the splitting between $4f_{5/2}$ and $4f_{7/2}$ in Ce. For core states, the spin orbit splitting can be very large. For example, the $2p_{1/2}$ and the $2p_{3/2}$ core states in W are split by 1351eV [18]. Important effects, such as the Kerr rotation in magneto-optical devices or the x-ray dichroism involve spin-orbit splitting. Therefore, a relativistic electronic structure theory is necessary. This is accomplished by solving the Dirac equations. Within a spherically symmetric potential, the Dirac equations, like the non-relativistic Schrödinger equation, can be decomposed into a radial and angular part.

The full correct treatment of the exchange and correlation in a theory is a difficult problem and has not yet been completely resolved. However, reasonable approximations are available.

Koelling and Harmon [14] have proposed a semi-relativistic (or scalar-relativistic) treatment. This approach involves an averaging over the spin-orbit splitting, but retains the kinematic effects. This restores most of the simplicity of a non-relativistic method but still gives an excellent representation of the core electron distribution and the appropriate (spin-orbit averaged) energies of the valence electrons.

2.1.5 Position File

To create a position file, the so-called POSCAR, for VASP, several problems have to be considered:

(i) matrix of the system
(ii) how many elements in the system
(iii) substitution or interstitial elements
(iv) strongly ordered or random ordered alloy
(v) positions of the elements
(vi) lattice parameters

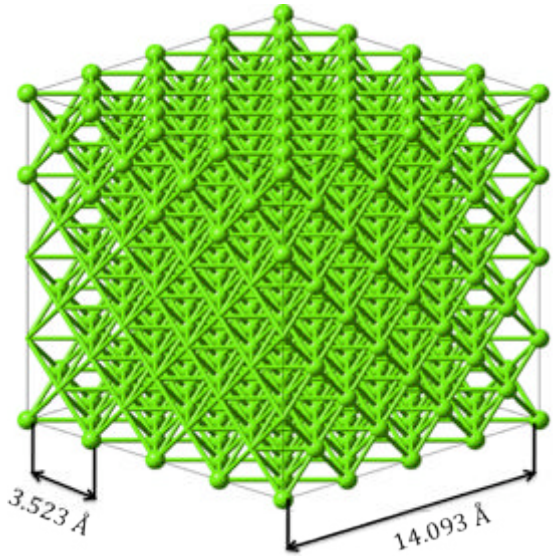

Figure 5: 4x4x4 super cell with a lattice parameter of 3.523[Å] and an overall length of 14.093[Å]

How those factors influence the position file is displayed in 4x4x4 nickel super-cell (Figure 5). The dimensions of a unit cell are 3.523 x 3.523 x 3.523 [Å] and consists of 4 Ni atoms. The creation of 4x4x4 nickel super-cell requires 4x4x4 unit cells next to each other, thus receiving a cuboid with a length of the edge of 14.093 [Å]. This cuboid consists of 256 Ni atoms in a simple P1 configuration and a lattice parameter of the unit cell of 3.523 [Å].

Appendix 1 and Appendix 2 show a direct comparison of a Ni and a Ni_3Al super cell. They are furthermore the files you need for the construction of a unit cell. To implement any impurity in this system, the lattice site of the impurity in cartesien coordinates must be calculated. Those coordinates are subsequently transformed in absolute coordinates, which then can be used by VASP. By implementing a point defect into the matrix the resulting energy is called “point defect formation energy” altered.

2.1.6 Input File

The input file or INCAR provides the VASP with the parameters necessary for starting and running the calculations necessary (Table-A 3).
The parameters of the INCAR file are provided by the individual task, which is supposed to be performed. It defines the step size, accuracy and other computation parameters. The compatability between the files is of outermost importance. Therefore, it has to be updated constantly in regards to the task and the computational environment. An INCAR file is designed for a 36 atom super cell with the same elements as a 256 atom super cell, however this is unlikely to work in a bigger system due to different requirements in step size, amount of electron and ions, and including other difficulties, which will occur while conducting calculations. An INCAR file designed for a large system might be working for a smaller super cell, yet possibly not deliver the required accuracy. Therefore it is very important that each INCAR file is specifically designed for it's tasks.

2.1.7 K - Point Grid

The Brillouin zone is of main importance for VASP calculations. Each Brillouin zone is different for various crystal structures (Figure 6) as it is a uniquely define primitive unit-cell of the crystal structure in reciprocal space. The first Brillouin zone is usually used for simulation calculations, nevertheless there are also a second and a third Brillouin zones, corresponding to a sequence of separated regions at increasing distances from the origin. Those zones are rarely used due to symmetry. Hence, the first Brillouin zone is often referred to as "the Brillouin zone". The Brillioun zone further defines a certain area with a distinct range of electron bands. Those band structures define several characteristics (electronic and optical characteristics etc.) of the material. They have different widths based on the atomic orbital's or maybe allowed to overlap in order to create a new larger single band (Figure 7).

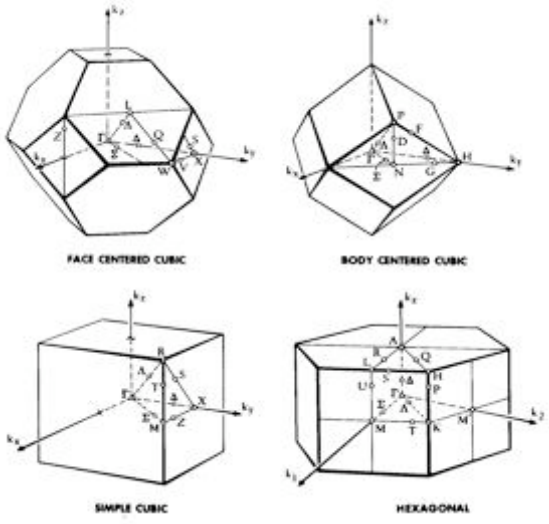

Figure 6: Brillouin Zone for different crystal structures. [15]

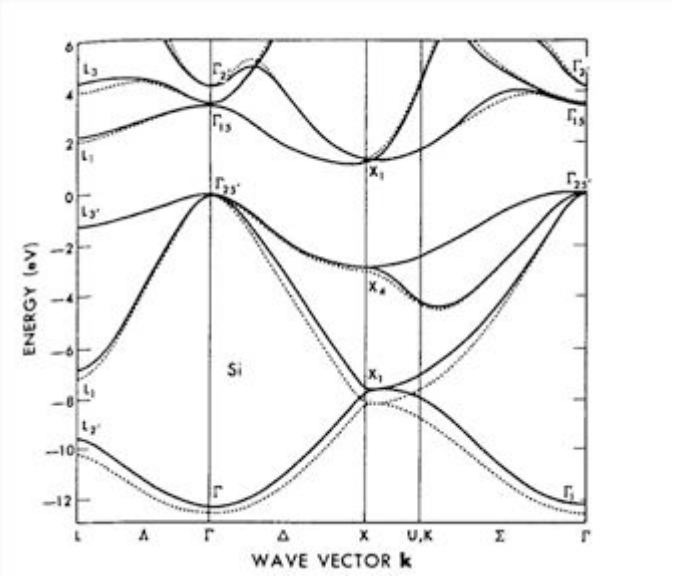

Figure 7: Illustration of electron bands and Brillouin zones in a material, in this case Si. [16]

The KPOINT file creates a k-mesh inside the first Brillouin zone to locate the parameters of the electron bands. The more accurate or finer the k-mesh (also known as k-grid) the more accurate are the obtained results. Until a certain point of accuracy is reached, all further steps in using a even finer k-mesh do not result in more accurate results, but in an increase of time which is necessary to calculate the system. The increased accuracy in terms of results is therefore not relevant.

2.1.8 Pseudo Potential File

The POTCAR file contains the pseudo-potential (alternatively called the effective potential file) for each atomic species, which is used in the simulation of the system. It is an attempt to replace the complicated effects of the core electrons motion and its nucleus with a simplified version (effective/pseudo potential), which is then used in the Schrödinger equation instead of the far more complex Coulombic potential (Figure 8).

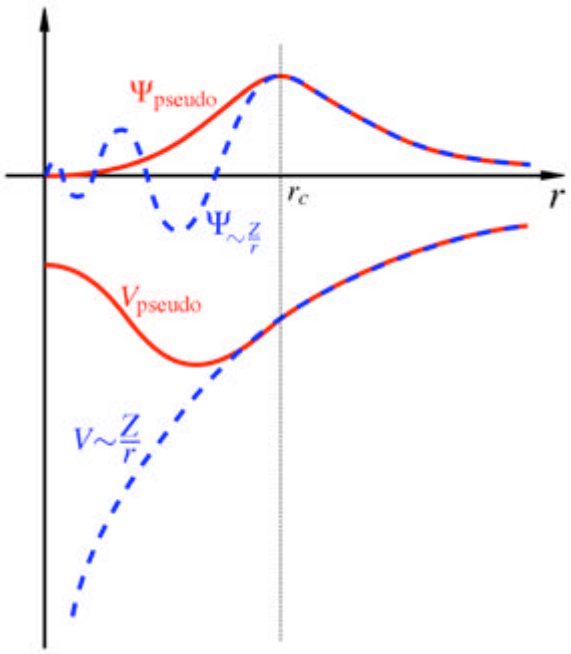

Figure 8: Comparison of a wave function in the Coulomb potential of the nucleus (blue) to the one in the pseudo potential (red). The real and the pseudo wave function and potentials match above a certain cutoff radius r_c [16]

The pseudo-potential deals only with the active valence electrons while the core electrons are considered to be a nucleus and are therefore excluded from the equation [17]. The cutoff radius does also play an important role in the realistic simulation of a material via the pseudo-potential file.

The higher the value of the cut off radius, the more accurate and realistic is the simulation shall be, however the gain of accuracy in the results obtained by the simulation has to be equalized with the amount of time lost. How r_c is determined can be seen in Table-A 4 and Table-A 5.

2.1.9 Methods

Convergence Testing and Lattice Parameters

The lattice parameters for pure elements are often well known, unlike those for multi-component systems. In order to achieve accurate and fast calculations those values are of outermost significance.

The KPOINTS and ECUT can already be determined by systems for pure elements, which saves time. In a multi-component system the ECUT is usually chosen from the highest ECUT value from all elements in the system and then increase by 25%. The KPOINTS are not altered as long as the system size remain. Later in the report the ECUT and the KPOINTS are going to be calculated for each specific system (Table-A 4 and Table-A 5).

If the lattice parameters for a system are already known, it is possible to save a huge amount of time in the ongoing calculations since the lattice for pure systems (single component or multi component system) is already close to the equilibrium. The cohesive energy, equilibrium lattice constant, and bulk modulus are determined by fitting the energy versus volume data to a Birch polynomial as shown in Figure 9.

$$V\left[\frac{Bohr^3}{Atom}\right] = \frac{A_{lat}^3}{0.148184534}$$

$$E\left[Rydberg\right] = \frac{E\left[eV\right]}{4 \cdot 13.60508}$$

$$Error = 1000000 \cdot \left(EFit - E\left[Rydberg\right]\right)^2$$

$$AlatEq = \left(4v_0\right)^{0.333} \cdot 0.529177$$

$$Bulk\,\mathrm{mod} = 14710.5164 \cdot k_o$$

Birch Fit convergence for NiAlO

	Alat [Å]	E [eV]	V [Bohr^3/Atom]	E [Rydberg]	E_{Fit}	Error
Birch Fit	3.400	-20.05996639	66.3092	-0.36861	-0.3686	4.68E-07
	3.425	-2.01E+01	67.7827	-0.37002	-0.3700	4.69E-07
	3.450	-2.02E+01	69.2779	-0.37098	-0.3710	4.70E-07
4 atoms FCC	3.475	-2.02E+01	70.7948	-0.37152	-0.3715	4.70E-07
	3.500	-2.02E+01	72.3338	-0.37169	-0.3717	4.33E-07
	3.525	-2.02E+01	73.8949	-0.37150	-0.3715	3.35E-07
	3.550	-2.02E+01	75.4783	-0.37105	-0.3711	2.11E-07
	3.575	-2.01E+01	77.0842	-0.37017	-0.3702	4.26E-08
	3.600	-20.05996	78.71266766	-0.36861	-0.3686	8.43E-08

VASP results are in eV and Angstrom

For Birch Fit we need Bohr and Ry

$Bohr^3$-> $Angstrom^3$

0.148184534

V_0	73.22457007	
E_0	-0.37179636	
k_o	0.00557876	
k_{op}	18.21846146	
AlatEq	3.5143	[Å]
BulkMod	82.066	[Gpa]

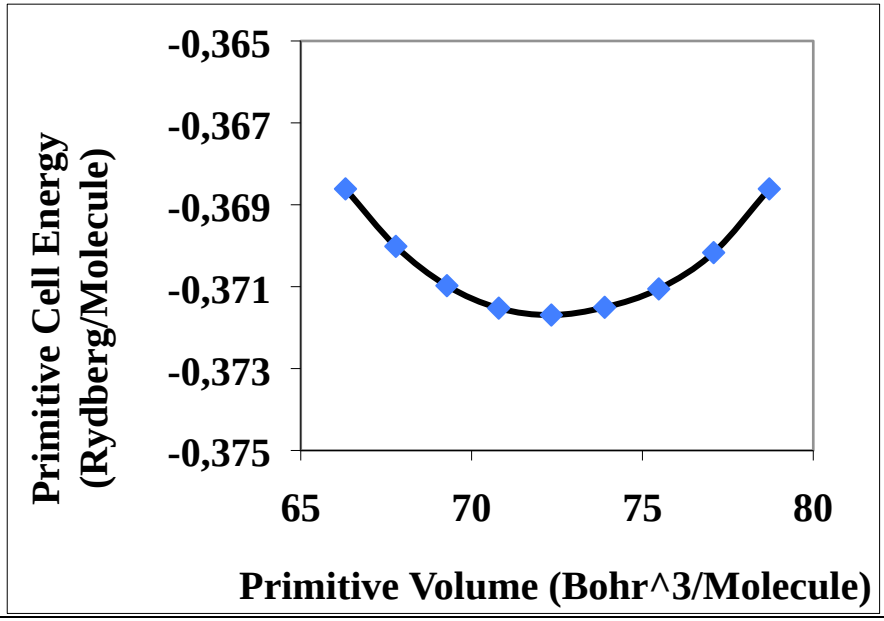

Figure 9: lattice convergence using a Birch Fit approach.

Point Defect Formation Energy

As a first step, the equilibrium of pure Ni_3Al (γ') and Ni (γ) was calculated. An interstitial impurity was later added to the system and calculated (Table 1). Ni_3Al has a L12 structure with octahedral Ni-rich, octahedral Al-rich, and tetrahedral interstitial sites. The data thus received helps to prediction possible locations for the interstitial impurity.

We considered the following additional impurities in our calculations: C, O for 3x3x3 cells. The cell size was chosen as a comparison for an anticipated 2x2x6 interface cell.

Point defect formation energy per atom:

$$E_{FP} = E_{Fp} - E_{F_1} - E_{F_2} \qquad (36)$$

E_{Fp} is the formation energy of a system with a point defect, E_1 is the formation energy of a pure system and E_2 is the formation energy of the element, which creates the point defect. As a result E_{FP} is the difference between a system with point defect and pure systems.

Table 1: Point Defect Formation Energy of Carbon in Ni_3Al. Values displayed are used in equation 36.

Point Defect Formation Energy

Ni_3Al	E_{Fi} (C) [eV]	E_{F1} [eV]	E_{F2} (Graphite) [eV]
2x2x2	-185.309	-177.454	-3.5443
E_{FP} [eV]	1.233		

2.2 High Temperature Corrosion

2.2.1 Carburization

In environments with high carbon concentrations and high temperature, two different kinds of carburization can occur.

CASE I: The carbon activity a_c is below one and a corrosive attack occurs due to internal carburization.

CASE II: The carbon activity a_c is below one and the environment has a carbon-enriched gas, which can lead to a metal wastage called “metal dusting”.

CASE I: Internal carburization

The corrosion attack occurs via carbon penetration of the outer material layers thus forming internal carbides. Those are most likely to form along the grain-boundaries, which serve as a diffusion path for carbon. Following consequences can be observed by internal carburization:

(i) a loss of ductility due to internal carbides
(ii) reduction of the melting point of the alloy
(iii) changes of microstructure due to an extensive formation of chromium carbides.

Internal carburization mainly occurs at high temperatures, above 1000 °C, and/or at low oxygen partial pressure, where it is not possible for the material to form a protective oxide layer.

CASE II: Metal Dusting

Metal dusting can be characterized by the disintegration of iron-, nickel- or cobalt based materials to a dust, which contains metal particles as well as carbon. Metal dusting frequently occurs in chemical plants during the reduction of hydrocarbons, methanol, ammonia etc. as well as in plants, where iron ore is reduced. General causes of this type of failures happen due to high concentration of CO-H_2 gas mixtures.

It is a rapid material wastage under any process condition where the activity a_c is higher than one.

2.2.2 Oxidation in Air

All materials suffer oxidation during exposure to air at high temperature. The corrosion rate or the corrosion resistance is heavily dependant on the amount of chromium and aluminum in the material. Chromium and aluminum is known to form thick and dense oxidation layers, which furthermore prohibit oxygen to diffuse deeper into the material.

$$4Al(s) + 3O_2(g) \rightarrow 2Al_2O_3(s)$$

$$4Cr(s) + 3O_2(g) \rightarrow 2Cr_2O_3(s)$$

Aluminum and chromium form a self-healing oxide-layer, which helps to protect the material from further oxidation due to its dense nature.

3. Experimental

Sample Preparation

In order to compare the results obtained by simulation, 3 different materials were chosen. H214, H214 aluminized (H214Al) and H1560.[1] H214 is a normal technical material, while the chemical composition of H214Al was chemically altered by aluminization (Figure 10). The material was annealed in 99% Al powder for 1hour at 950 °C and later heat-treated at 1050 degrees C for 190 hours. The material was aluminized to achieve a direct comparison in the behavior of carbon and oxygen corresponding to the aluminum content. The aluminum content was investigated using RFA. H1560 is an experimental Ni based single crystal. Thus it can be utilized as a comparison to the simulation, due to its ordered microstructure and the aluminum content of at least 25 atom percent.

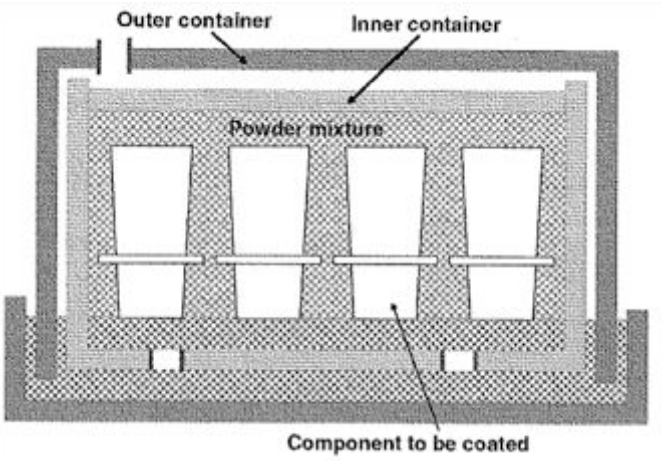

Figure 10: Schematic diagram of an apparatus used for aluminizing by pack cementation. [19]

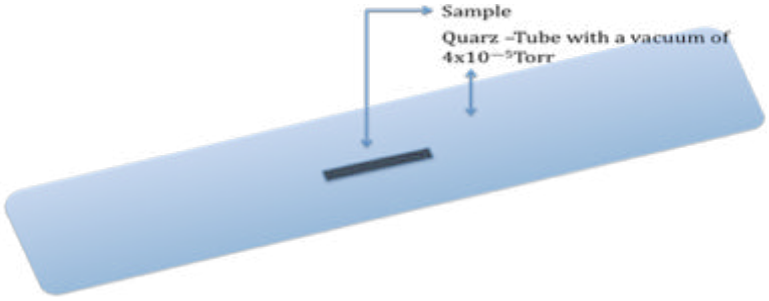

Figure 11: Quartz-Tube with a sample and a vacuum of $4x10^{-5}$Torr. The sample is positioned horizontally in the tube, which is ordered horizontally as well in the furnace.

The samples were polished to a surface roughness of 0.25µm, coated with a graphite spray and encapsulated in quartz at a vacuum of $4x10^{-5}$Torr. A second pair of samples, where encapsulated in quartz at a vacuum of $4x10^{-5}$Torr as well, however this time without the graphite coating in order to serve as reference samples (Figure 11 and Figure 12).

[1] Dr.Stuart Maloy and Dr. Sara Perez-Bergquist provided the materials and the history of the materials.

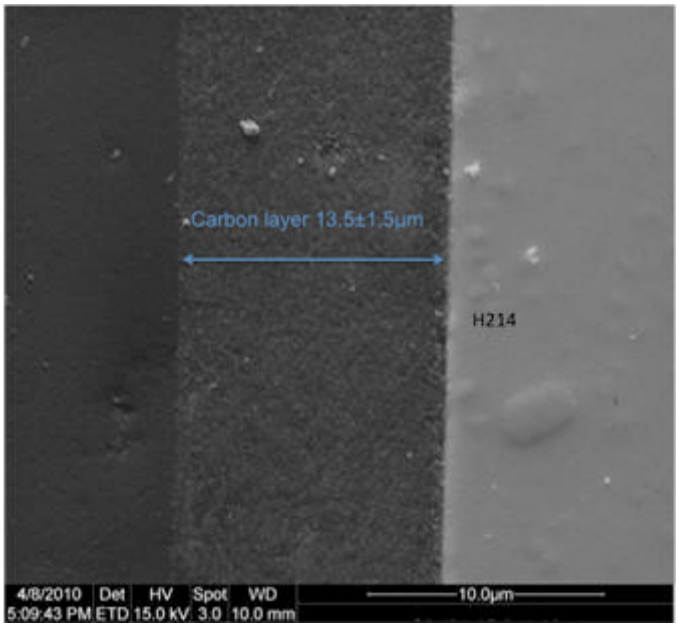

Figure 12: H214-sample with an average Carbon layer thickness of 13.5±1.5µm. The surface of the sample was polished to a surface roughness of 0.25µm.

The average thickness of the graphite coating was determined by way of a sample, which was produced solely for this purpose and characterized using SEM, to be 13 ±1.5µm (Figure12). Henceforth, the samples were immersed in Epoxy and coated with a 20nm thick conducting layer. The samples were further heat treated for 1000 hours at a temperature of 750 °C, which is a common operating temperature for a turbine of a military aircraft and for comparison of the diffusion rate. A second heat-treatment was conducted at a temperature of 1000 °C for 48 hours.

To observe the grain-boundaries and the γ – γ' interface the samples were etched in an acid consisting of 33% water, 33% Acetic acid (CH_3COOH), 33% Nitric acid (HNO_3) and 1% Hydrofluoric acid. The samples had to be etched for up to 30 minutes.

To achieve a rough diffusion path of Carbon in the samples, EDS-characterization and a SEM characterization were used additionally as an optical microscopy. To characterize the behavior at interfaces, STEM samples were cut from locations, which were chosen using SEM and an optical microscope.

4. Results

4.1 Simulation Results

Initially, the point defect formation energy per atom for Carbon and Oxygen in a pure Ni single crystal was calculated (Graph 1). The calculated results in Graph 1, it allows for a first prediction that oxygen has a higher affinity to pure nickel than carbon does. The different lattice position for oxygen is not as significant unlike in the case of carbon, due to the fact that there is only a difference of 0.003 [eV] per atom between the lattice sites. In contrast carbon does have a difference of 0.037 [eV] per atom between a tetrahedral and an octahedral position.

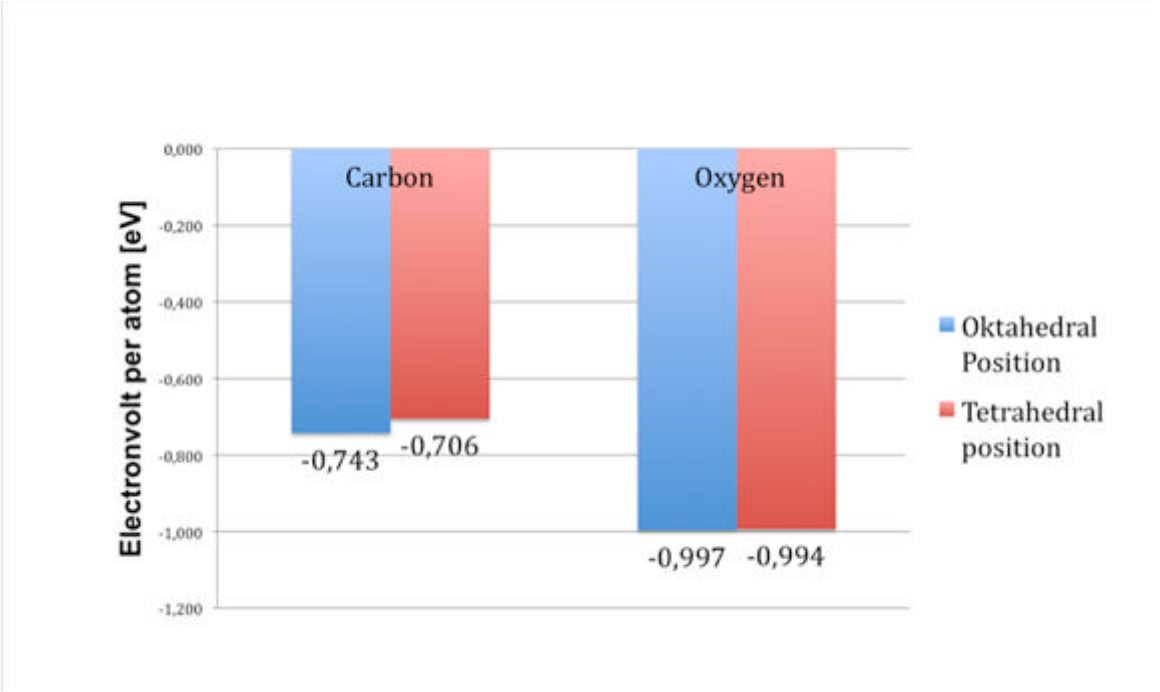

Graph 1: Point defect formation energy per atom of a 3x3x3 (108 atoms) super-cell for a pure Ni system with one interstitial element (carbon or oxygen) at different lattice positions.

The negative value indicates that the reactions with the interstitial elements might be spontaneous, therefore it can be beneficial for the formation energy of the system. A system is always driven by the need to achieve the most stable energetic formation, which is considered the lowest energy level.

While in a pure Ni-system, the distinction between the elements might be minor, the difference for a Ni_3Al system is much greater (Graph 2). The point defect formation energies are positive, which suggests that energy must enter into the system to induce an interstitial atom into the system. The atom is forced into the crystal lattice reducing the stability of the formation.

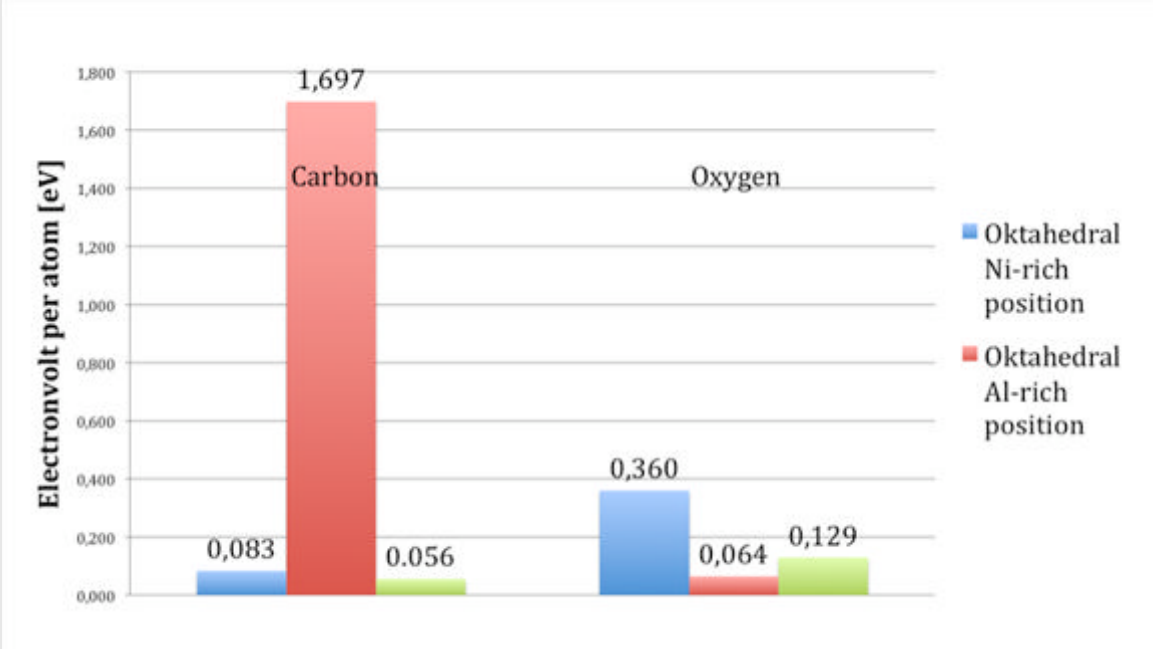

Graph 2: Point defect formation energy per atom of a 3x3x3 Ni_3Al (108 atoms) super cell and one interstitial element (carbon or oxygen) at different lattice site positions.

The values obtained by the simulation indicate that carbon prefers a Nickel rich area compared to an aluminum rich lattice site position. The energy of 1.667 [eV] is required to force a Carbon atom close to an aluminum rich lattice site. This is a huge amount of energy, indicating that carbon is trying to avoid any aluminum rich lattice site positions. Oxygen on the other hand shows a huge affinity to aluminum, which results in the lowest point defect formation energy at an aluminum rich position or a lattice site close to aluminum. During the experiment, oxygen is drawn to Aluminum in order to form an Al_2O_3 layer inside the material or close to the surface while Carbon is trying to avoid Aluminum rich positions.

4.2 Experimental Results

For the experimental study of the behavior of carbon and oxygen, three materials were selected. H214 was chosen due to it's high aluminum content, the aluminum content was even increased by aluminizing H214. This allows for a display of the impact of aluminum on the behavior carbon and oxygen. An experimental material H1560 was utilized due to it's high content of aluminum and its single crystal structure (morphology).

The element's behavior was tested at the material operating temperature of 750 °C for 1000 hours and at a much higher temperature of 1000 °C for 24 hours.
The samples were characterized using optical microscopy, scanning electron microscopy (SEM) and energy dispersive X-ray spectroscopy (EDAX). Samples, which showed high activity of Carbon and Oxygen at the grain boundaries, were further distinguished, using focused ion beam (FIB) and STEM.

Table 2: Chemical composition of H214 and H214Al. Note that the aluminum content in H214Al is nearly twice the amount than in H214.

H214

Nominal chemical composition in weight percent									
Ni	Cr	**Al**	Fe	Mn	Si	Co	C	B	Y
75	16	**4,5**	3	0,5	0,2	0,1	0,05	0,01	0,01

H214Al

Nominal chemical composition in weight percent								
Ni	Cr	**Al**	Fe	Mn	Si	Co	Ti	Mo
76,5	12,3	**9,36**	1,51	0,15	0,04	0,1	0,04	0,04

4.2.1 H214 and H214Al exposed to Carbon

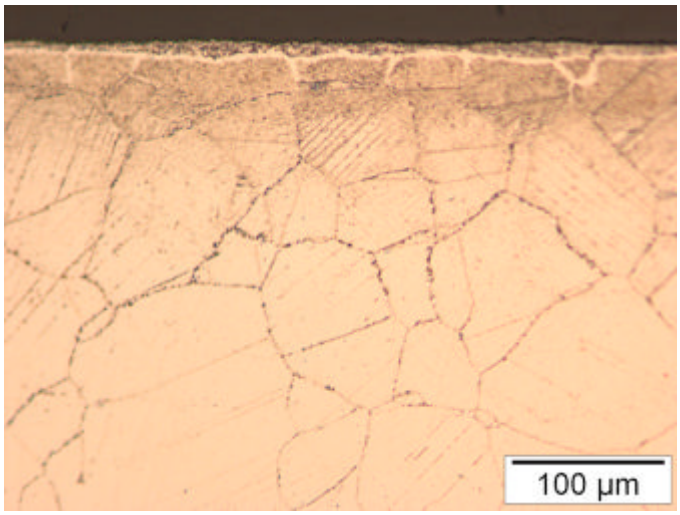

Figure 13: H214 coated with Carbon annealed at 750 °C for 1000 h.

The Carbon diffused along the grains into the material. In this case, the diffusion alongside the grains was so rapid that traces of Carbon were found all over the material. The Carbon further diffused based from the grain boundaries into the grain itself. The Carbon diffusion had a higher impact on the grains close to the surface, than on those closer to the core of the material. Due to the diffusion of carbon alongside the grain boundaries, chromium segregated to the grain boundaries. In addition to a carbon and chromium rich region, a nickel-depleted region was created. This behavior was verified by element maps (Figure 14) and line-scan (Figure 15, Graph 3).

This form of carburization can be often found in environments of low oxygen pressure, where carbon diffuses alongside the grains into the material and forms $M_{23}C_6$ (in this case $Cr_{23}C_6$, Carburization first class).

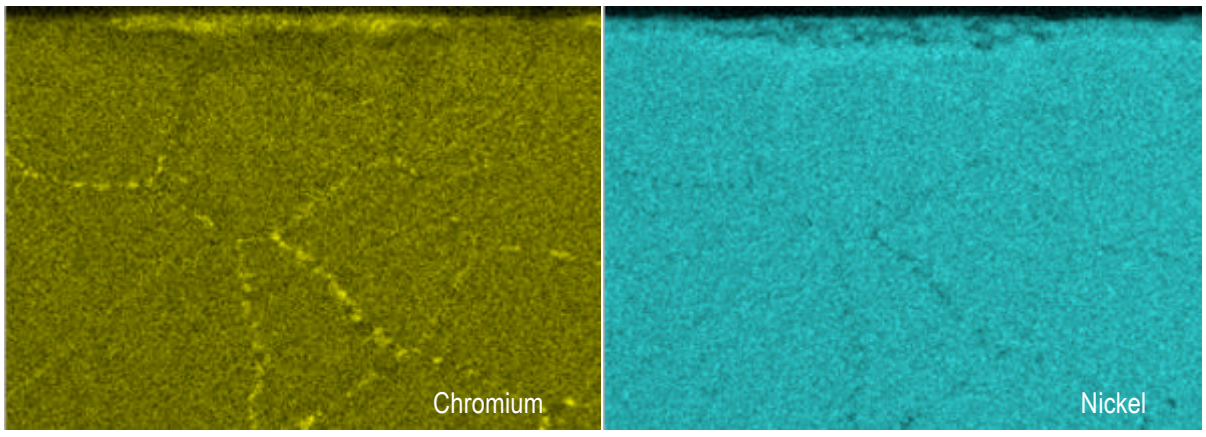

Figure14; Chromium and nickel distribution in H214 (C 750 °C 1000h). Note the higher density of chromium as well as the nickel depletion at the grain boundaries.

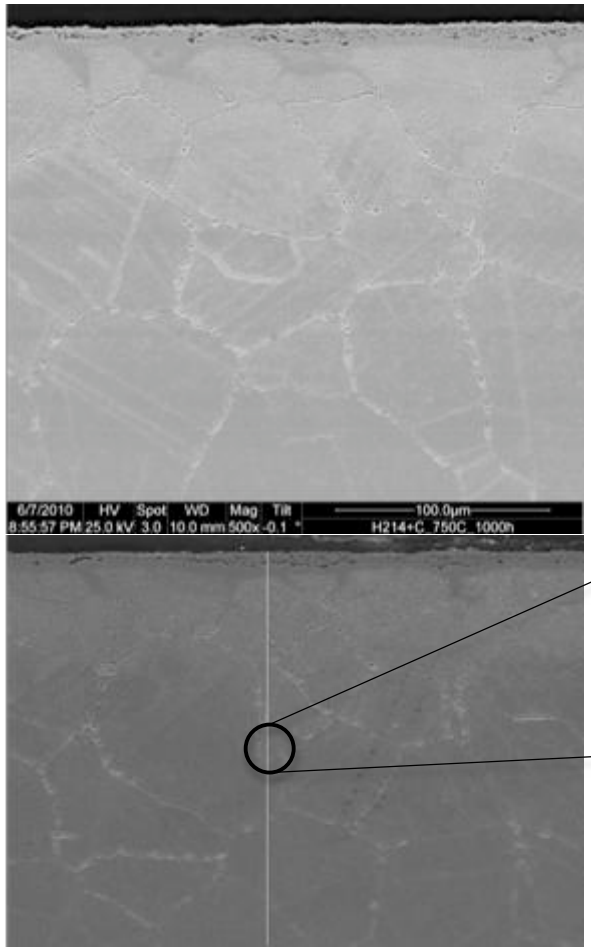

Figure 15; Line-scan of H214 coated with Carbon and annealed at 750 C for 1000 hr. Note the chromium segregations at the grain boundaries.

The line-scan of H214 Carbon (which was coated and annealed at 750 °C for 1000 hr), displays a rapid and significant increase in the chromium content at each grain boundary, while the nickel content is decreasing. While some carbon spikes can be observed, carbon and oxygen are

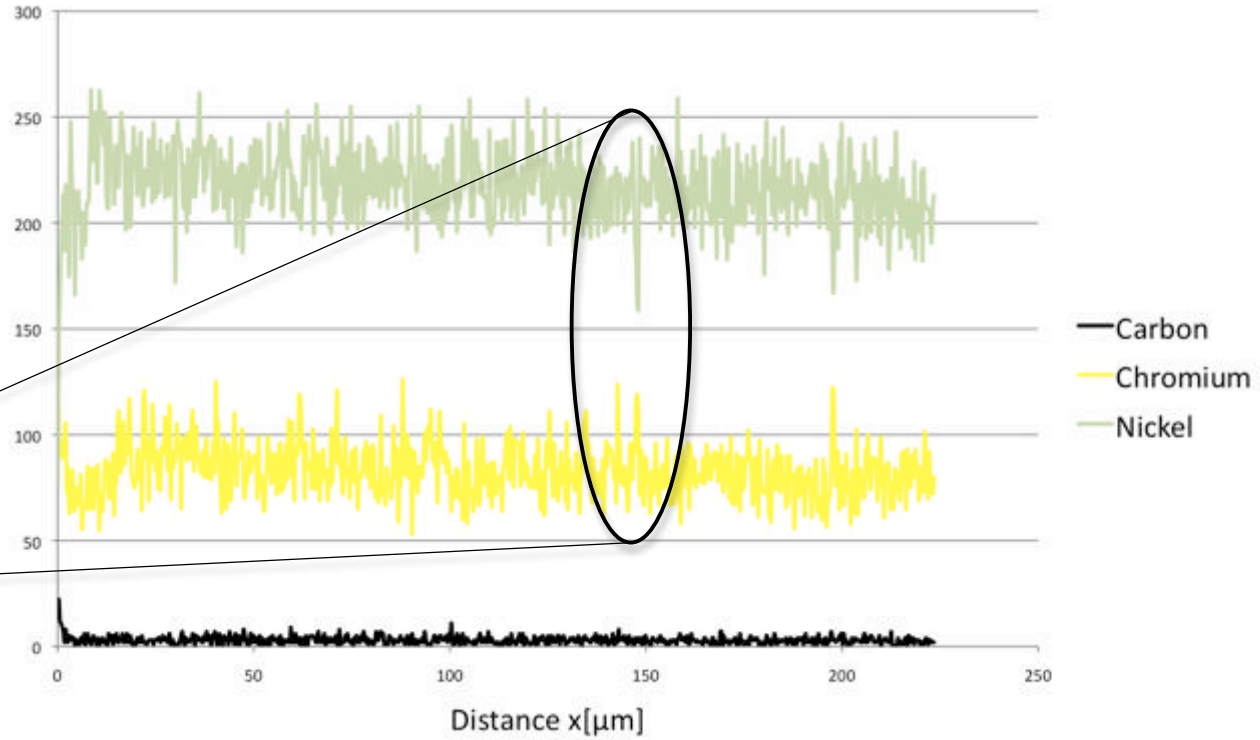

Graph 3: Displayed is the line-scan of H214C 750°C 1000 hr. Note the marked areas each time the line-scan crosses a grain boundary. The nickel content is decreasing while carbon and chromium content is increasing.

unfortunately hard to detect with the energy dispersive X-ray spectroscopy. Nickel depletion at the grain boundaries and a chromium and carbon increase can be observed, which suggest that $Cr_{23}C_6$ precipitates were formed at the grain boundaries.

The diffusion behavior of Carbon in H214Al is different to its behavior in H214. In H214 carbon diffused alongside the grain boundaries. For the diffusion of carbon in H214Al two aspects have to be taken into account for the diffusion process:

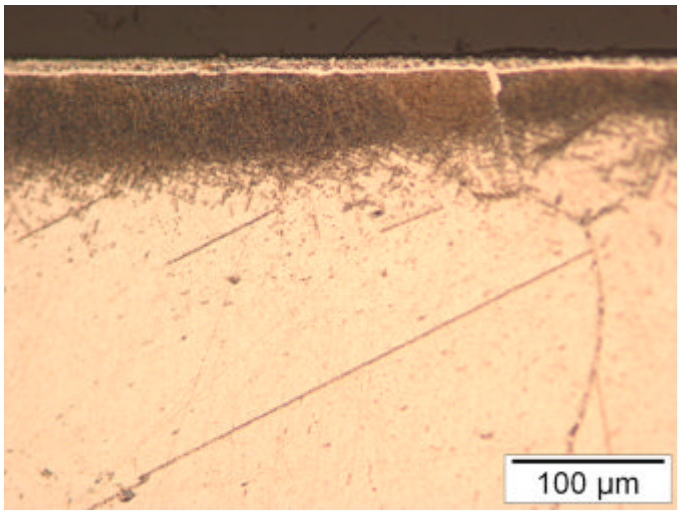

Figure 16: Diffusion front of carbon in H214Al (H214 aluminized) carbon coated and annealed at 750 °C for 1000 hr.

(i) as seen earlier, carbon does have a high disaffirmation towards aluminum

(ii) carbon was able to diffuse so fast into the material due to the fine grain. Alternatively, H214Al does have a much larger grain and forces carbon to diffuse into the bulk much earlier than H214 did.

Carbon is forming a diffusion front, in the **aluminized Hasteloy 214 (H214Al)**, starting from the surface into the grain (Figure 16).

Although a concentration of chromium can be detected in the EDAX maps (Figure 17) of H214Al, it seems lower than in H214. It could thus be the reason for a higher aluminum content and the dislike of carbon as noted earlier in this thesis. As other elements such as silicium hinder the diffusion of carbon by forming precipitates like silicium-carbides, aluminum appears to force carbon to a different pathway due to its imparity.

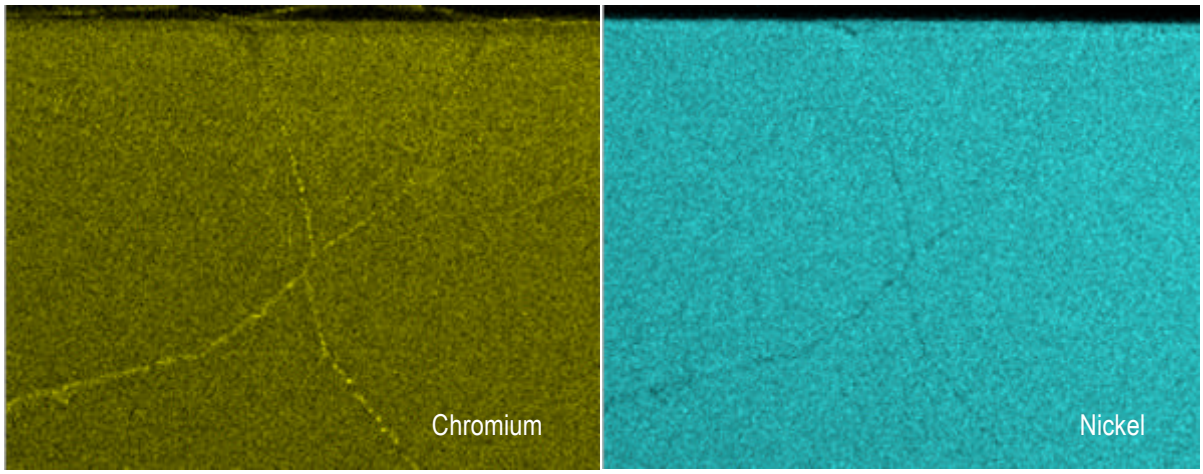

Figure 17: EDAX map of H214Al, showing the distribution of chromium and nickel.

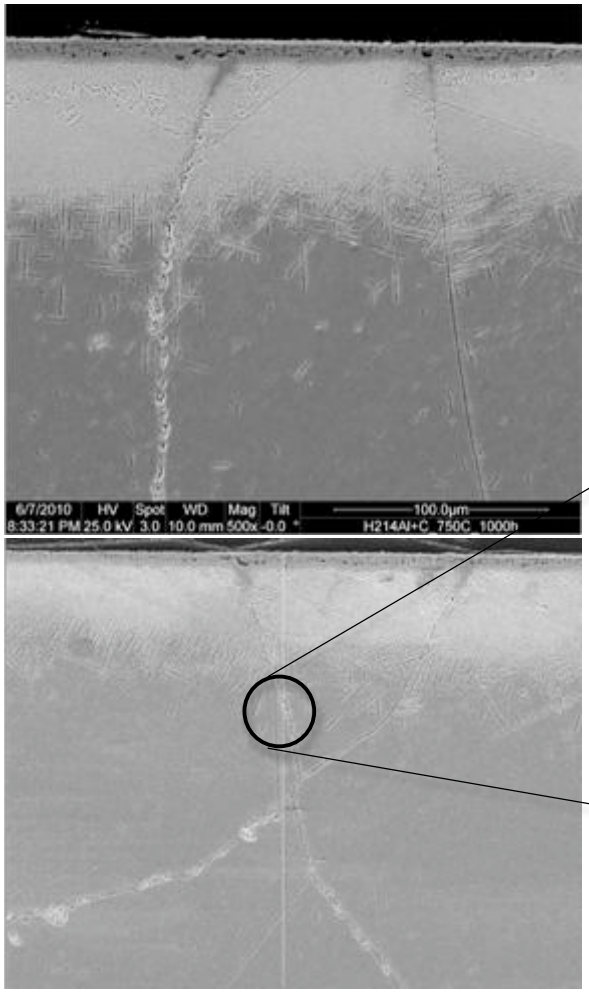

Figure 18; Line-scan of H214Al coated with Carbon and annealed at 750 °C for 1000 hr.

Albeit the diffusion of carbon is mainly from the surface into the bulk, chromium carbides have been formed at the grain boundaries. Each time the scan crossed a grain boundary the chromium content increase significantly, while the nickel content dropped.

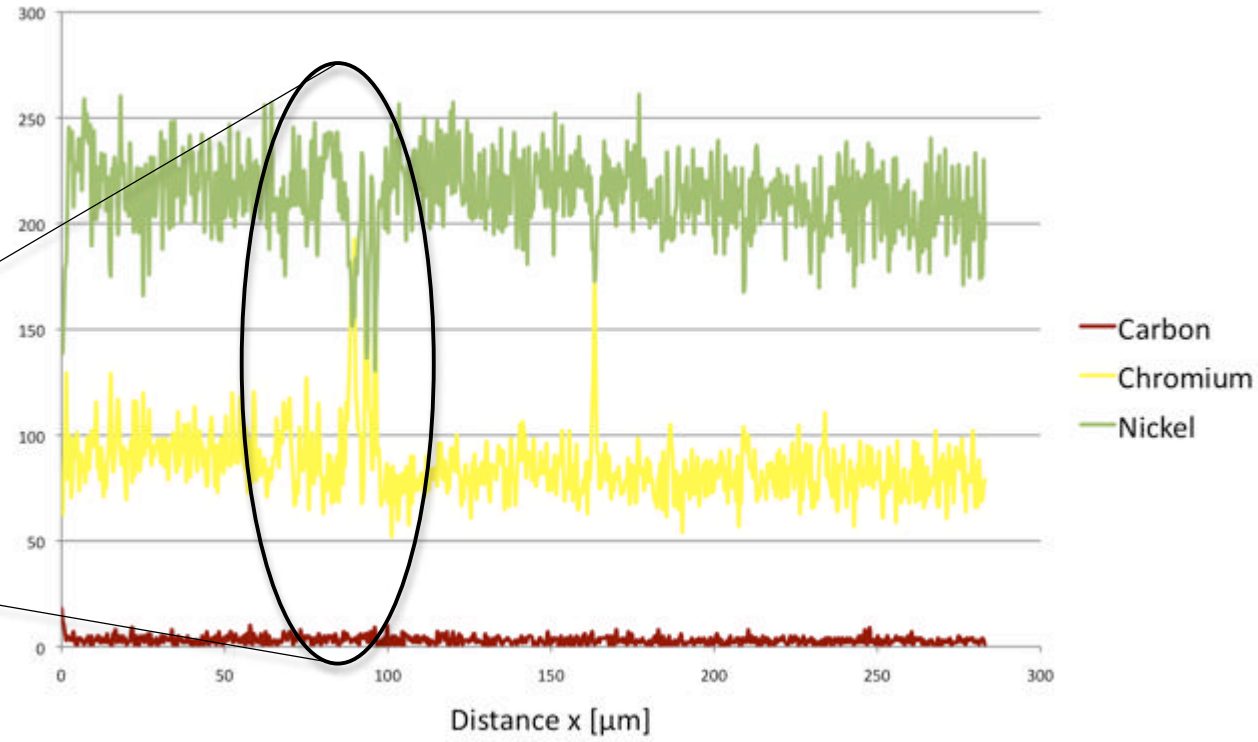

Graph 4: The nickel depletion as well as the increase of chromium is clearly visible when the path of the line-scan is crossing a grain boundary.

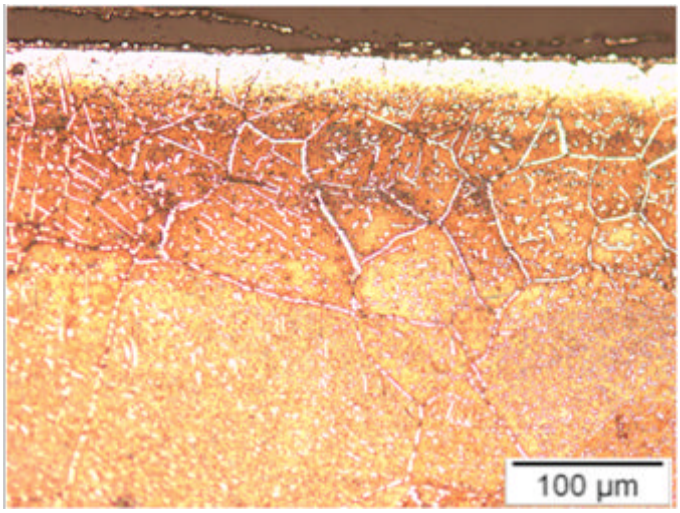

Figure 19: H214+C annealed at 1000 °C for 24 hours. Note the higher carburization effect in the sample caused by increasing the temperature about 250 °C.

The temperature ranges were increased from the operating temperature (750 °C) to a much higher temperature (1000 °C) to show the effect of temperature on the diffusion constant and to have a direct comparison between the interstitial element behavior at different temperatures.

The diffusion constant is linked to the temperature as can be seen below:

$$D = D_0 \exp\left(-\frac{Q}{kT}\right)$$

and in Figure 19. At 750 °C H214 not only the grain boundaries were effected but also the whole bulk itself. The element map detected huge areas of chromium segregations and nickel (Figure 20) depleted areas, which were later also detected at the line scan (Figure 21). In order to receive a better understanding of those segregations, an area around a grain-boundary was chosen and characterized using FIB and STEM.

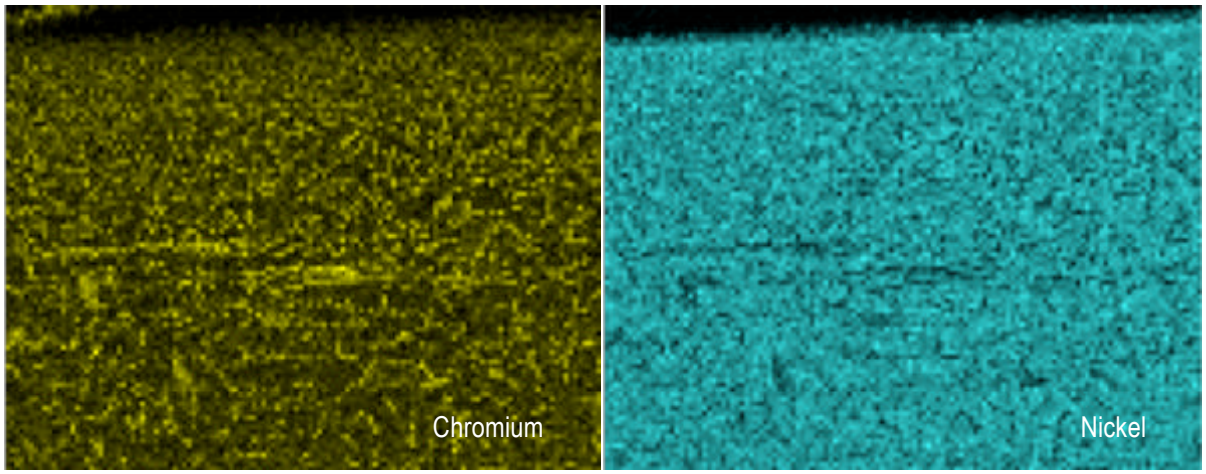

Figure 20: Element map of H214+C annealed at 1000 °C showing chromium and nickel concentrations.

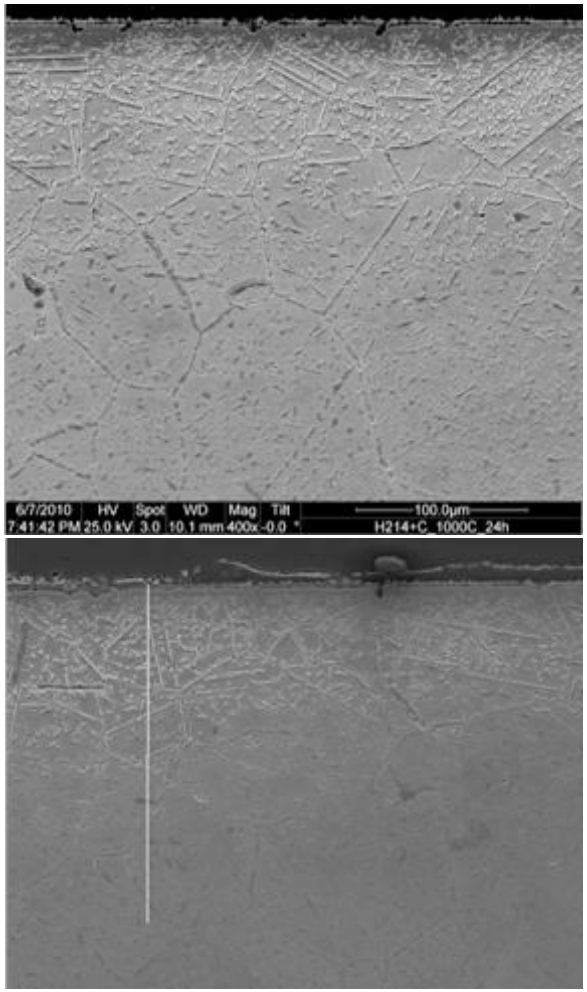

Figure 21: Line-scan of the effected area in H214+C annealed at 1000 °C for 24 h.

As already seen in the previous element maps, carbon affects both the grain-boundaries and even the bulk of the material itself.

Graph 5: The chromium-carbides are clearly visible due to the drastic decrease of nickel and the chromium spikes.

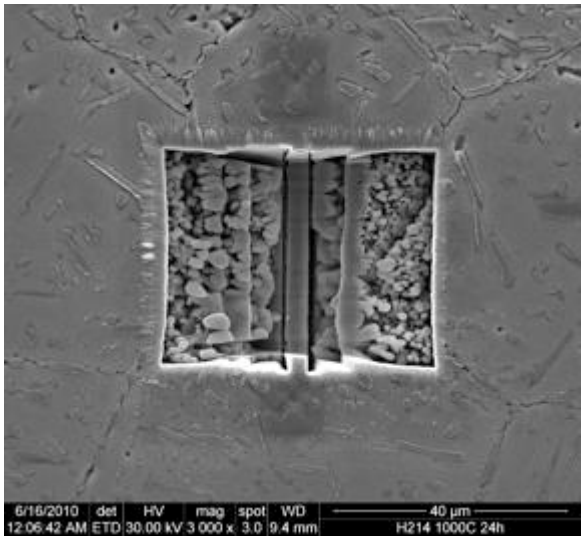

Figure 22: Area chosen from H214+C annealed at 1000 °C for 24 h in order to conduct a STEM characterization.

In order to characterize the particles, which are supposed to be $Cr_{23}C_6$ a FIB in STEM mode was used. An area of a grain boundary was chosen and prepared, which includes coating the surface with a protective layer and later cut it out, using the ion beam of the FIB (Figure 22). In the next step, the sample was welded onto a sample-holder and a search was conducted for the best spot for an EDAX characterization (Figure 23).

As soon as this location was found, an EDAX scan was performed and used for a more precise characterization (Figure 25). By using the EDAX in point characterization mode, it was possible to determine the chemical composition of the particles plus the matrix surrounding it. The results can be seen down below in table 3.

Due to the high carbon background recording the carbon content and the accuracy of other elements cannot be considered consistent.

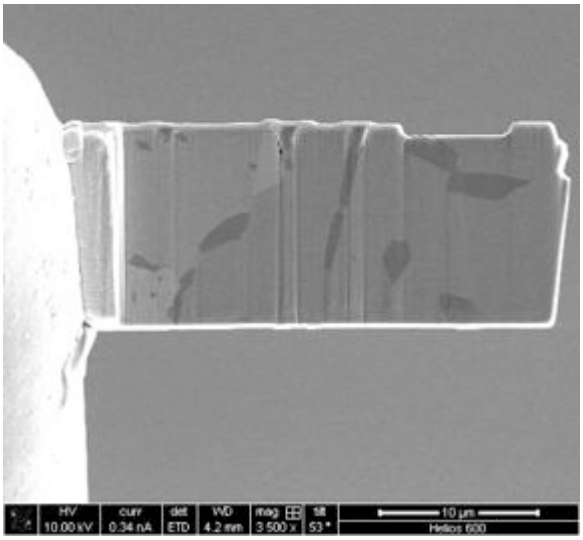

Figure 23: H214+C at 1000 °C for 24 h sample prepartation for STEM.

Therefore, the results received from EDAX measurements must be used with care.

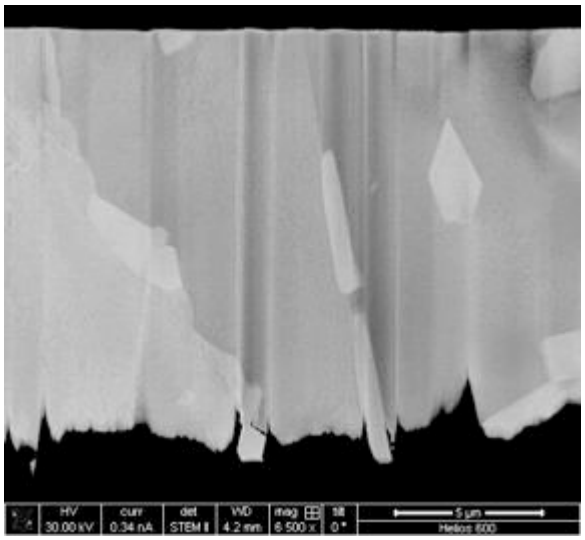

Figure 24: H214+C at 1000 °C for 24 h characterized by FIB in STEM mode.

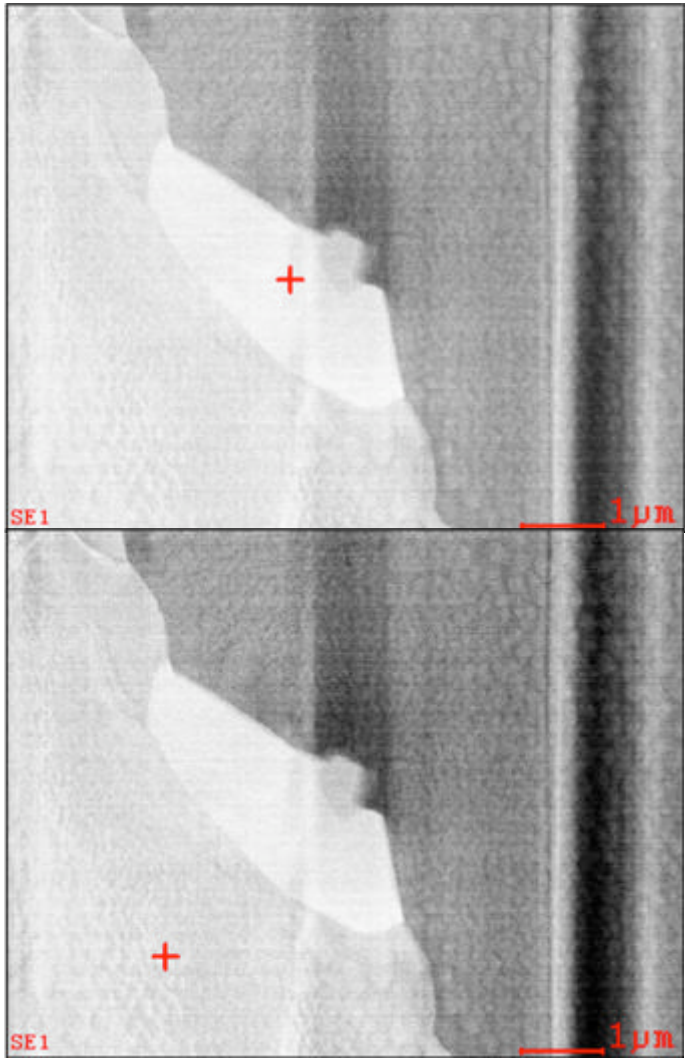

Figure 25: $Cr_{23}C_6$ particle and Matrix in H214+C at 1000 °C for 24 h. The pictures display the areas used for the EDAX characterization. (a particle embedded in H214 and the matrix of H214 itself as well).

Table 3: Elemental composition as received from EDAX point characterization. The data provided below was retrieved by EDAX characterization of the areas shown to the left.

Element	Wt%	At%
C	53,19	80,88
Al	6,73	4,55
Si	2,05	1,43
Cr	34,96	12,28
Ni	3,07	0,95

Element	Wt%	At%
C	45,49	75,71
Al	11,66	8,64
Si	2,71	1,93
Cr	4,34	1,67
Fe	1,05	0,38
Ni	34,29	11,68

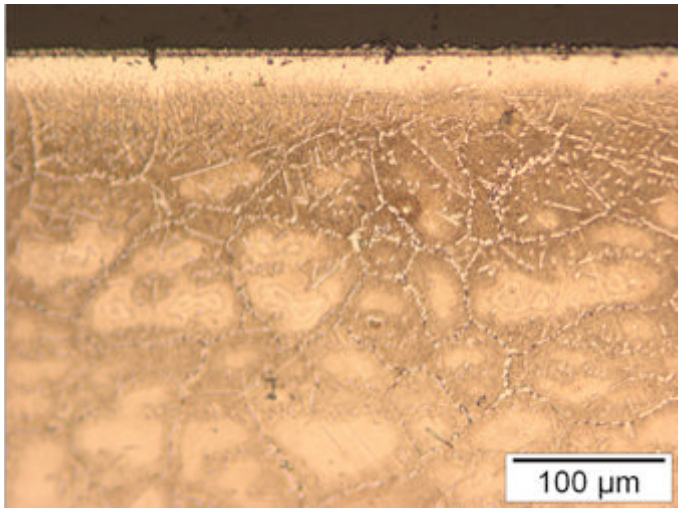

Figure 26; H214Al+C annealed at 1000 °C for 24 hours. Note, that the bulk regions of the grains are not as affected by the carbon diffusion as in sample H214.

While in H214 a massive amount of carburization of the first class could be observed, there was only minor carburization in the aluminized H214 (Figure 26). Although the carbon diffused through the whole sample alongside the grain boundaries, it didn't affect the bulk of the material as much as it did in H214. This result can be predicted by the simulation of the bulk system, where carbon needs a much higher energy level in order to be introduced into a system with higher aluminum content unlike a system with no aluminum present.

There was no major change in the elemental map of aluminum or nickel observed, however it is obvious that the chromium does not have such a high concentration at the grain boundaries as in the previous samples (Figure 27). A line-scan was conducted, confirming that the segregation of chromium in H214Al was not as severe as before (Figure 28 and Graph 6). In order to conduct a STEM and EDAX characterization of the particles found at the grain boundaries, a TEM foil was cut out using the ion beam microscope (Figure 29).

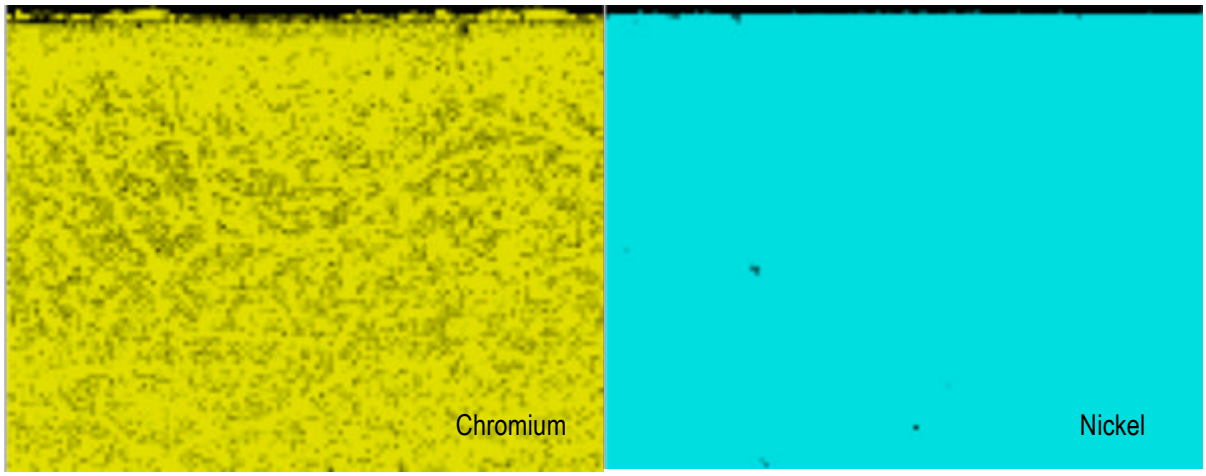

Figure 27; Elemental map of chromium in H214Al annealed at 1000 °C for 24 hours. It appears that the segregation of chromium to the grain boundaries are not as major as In the previews samples while can be no significant changes observed in nickel.

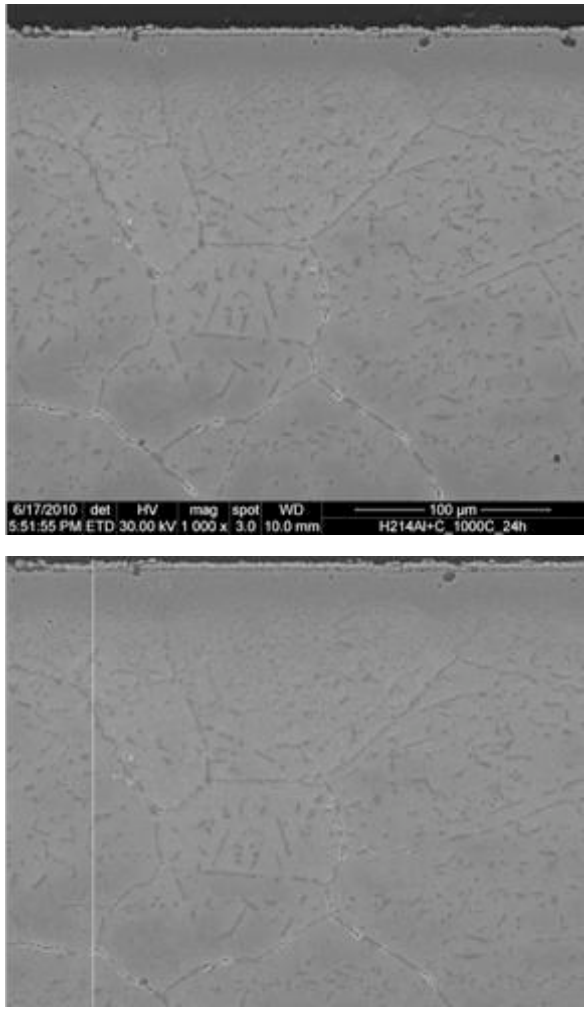

Figure 28: illustrated is the sample area used for a line-scan for an element characterization in H214Al annealed at 1000 °C for 24 hours

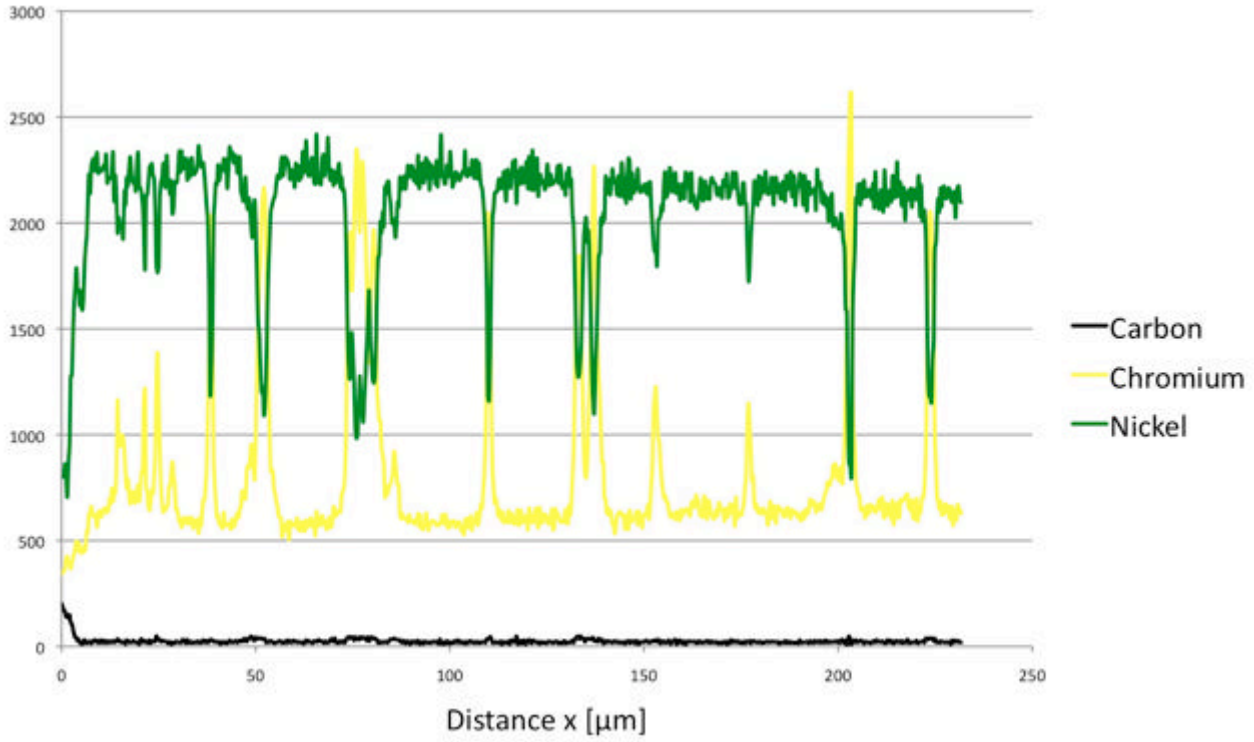

Graph 6: Each time the line-scan path crosses a chromium-carbide, it is clearly visible due to the drastic decrease of nickel and the increase of chromium.

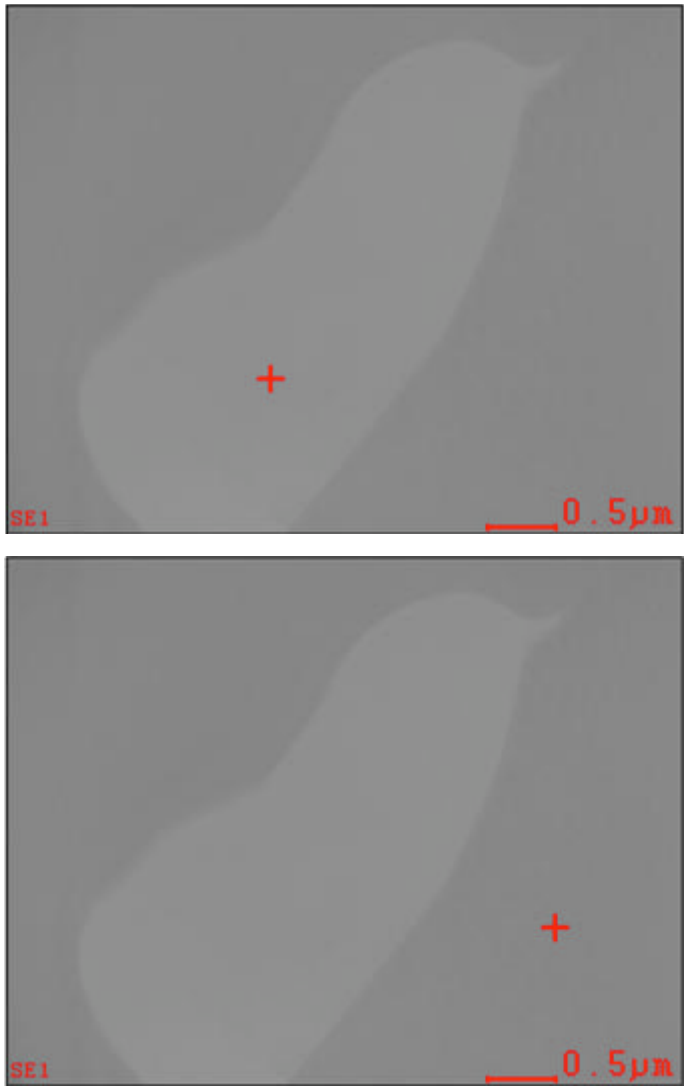

Figure 29: EDAX characterization of a particle in H214Al and of the H214Al - matrix annealed at 1000 °C for 24 h.

Table 4: Data received by EDAX characterization. The characterization location I shown on the left hand side.

Element	Wt%	At%
C	51,46	79,15
Al	8,82	6,05
Si	2,74	1,80
Cr	33,86	12,03
Ni	3,13	0,99

Element	Wt%	At%
Al	26,33	41,43
Si	5,82	8,80
Cr	6,87	5,62
Fe	1,82	1,38
Ni	26,44	17,67

4.2.2 H214 and H214Al exposed to Oxygen

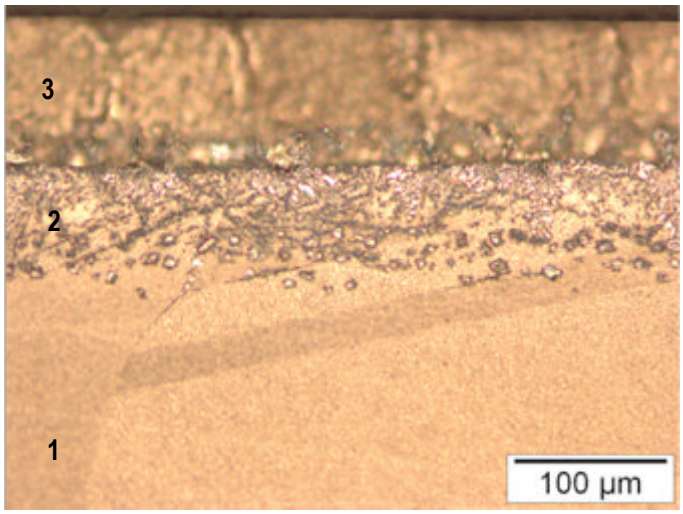

Figure 30: H214 annealed at 750 C for 1000 hours at air. It can be clearly seen that the oxidation produced three zones inside the material, which can be characterized as followed;

1. The unaltered bulk material
2. A chromium rich and a nickel depleted zone
3. A thick nickel and aluminum oxide layer.

Carbon is diffusing into the material using grain-boundaries and later into the grains themselves. The diffusion of oxygen works differently however. As observed from the simulation, oxygen has a high affinity to pure nickel aside a preference for aluminum reach positions. Additionally, it's also known that oxygen is forming stable aluminum and chromium oxide layers. Those layers do protect the material from further oxidation due to their dense nature. It was observed that nickel started diffusion outside, forming a thick layer of nickel oxide. After forming this first diffusion barrier the diffusion of oxygen was slowed down as it had to penetrate the nickel oxide layer first and then diffuse deeper into the material hitting aluminum and chromium atoms and forming a second, denser barrier of aluminum and chromium oxide inside the material (Figure 30).

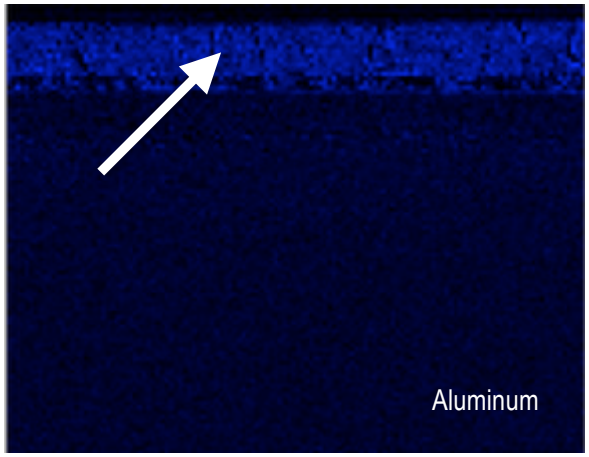

Figure 31: Element map of aluminum in H214 exposed to air at 750 °C for 24 hours. Notice the thick aluminum layer towards the surface while it seems that all though the aluminum concentration on the surface is much higher than in the bulk, there seems to be no gaps of aluminum.

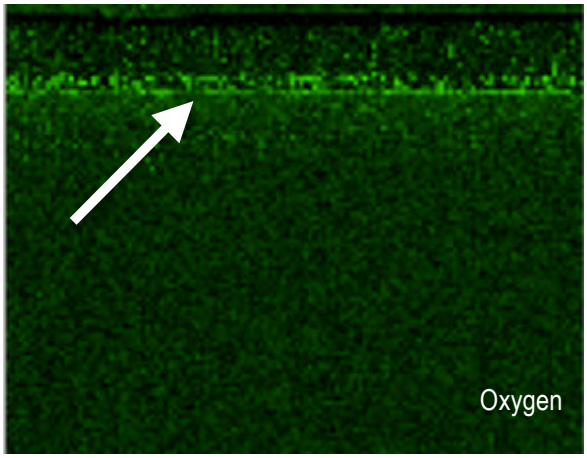

Figure 32: Oxygen distribution in H214 annealed at 750 °C. Note the thick layer of oxygen in marked area and the later decreasing content deeper into the bulk. Due to the fact that oxygen is rather difficult to detect and that there is a high oxygen background dedection the oxygen shown in area two can be considered a background fragment.

Elemental maps allow to visualize the diffusion process better (Figure 31-34). In Figure 49 a Kirkendall effect can be observed, which is caused by the fast diffusion of nickel and chromium to the surface (Figure 33 and Figure 34). This result is later confirmed using a line scan. The line scan also unveils how deep the material is affected by the rapid diffusion of nickel and chromium towards to surface (Figure 36, Graph 7). Graph 7 illustrates the elemental distribution inside the material. While all changes are happening in the first 150 µm of the bulk, the rest of the material seems unaffected by any changes caused by diffusion. It appears that nickel cannot diffuse quickly enough from the bulk to the depleted areas close to the surface, thus leaving empty spaces. Those vacancies are instead filled by chromium and aluminum. Overall, there are two different oxide layers; the first consists mainly of nickel and aluminum oxide while the main components of the second layer are a chromium and an aluminum oxide-layer.

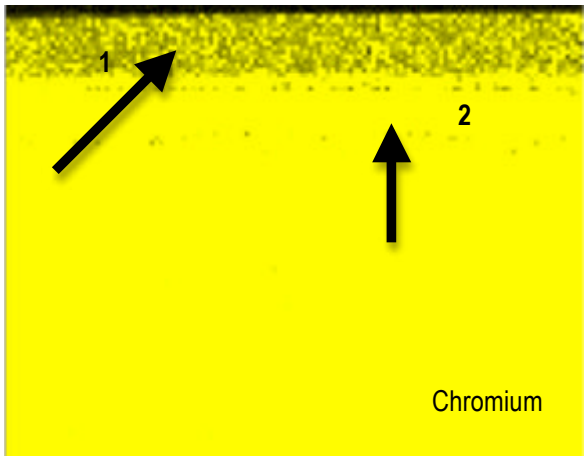

Figure 33: While chromium is evenly distributed throughout the material, it's density at the surface is much lower (1) than in the other bulk material and it appears to create a Kirkdall effect (2) by diffusion to faster to the surface than the bulk can reoccupy the empty lattice pace and by forming Cr_2O_3.

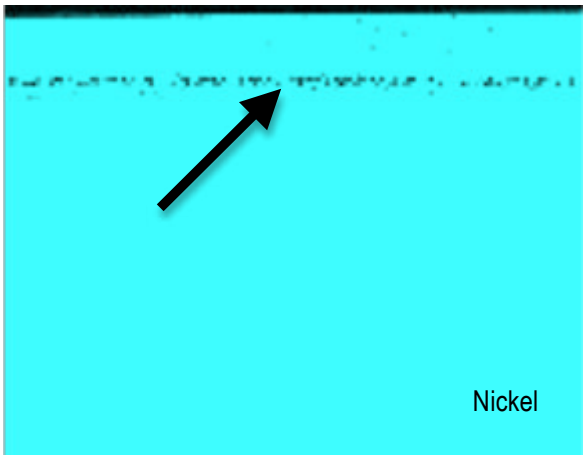

Figure 34: Nickel diffused faster to the surface and formed NiO than it could diffuse from the bulk to the nickel depleted region. Therefore a Kirkeldall effect occurred which is visible with the optical microscope as well as is clearly visible in the EDAX characterization.

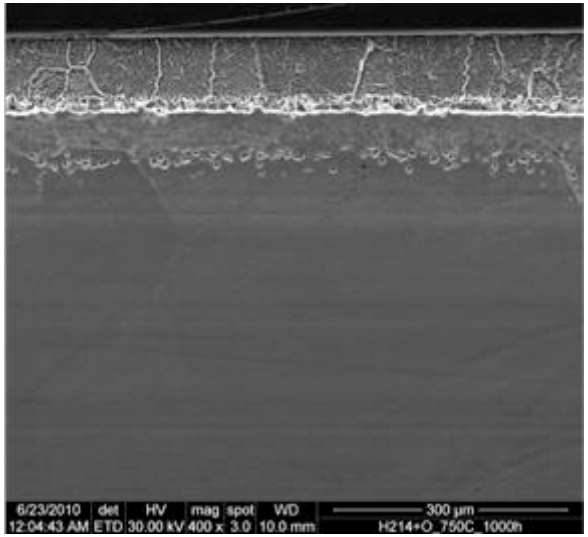

Figure 35: Area chosen to conduct the elemental line-scan for H214 annealed at air at 750 C for 1000 hours.

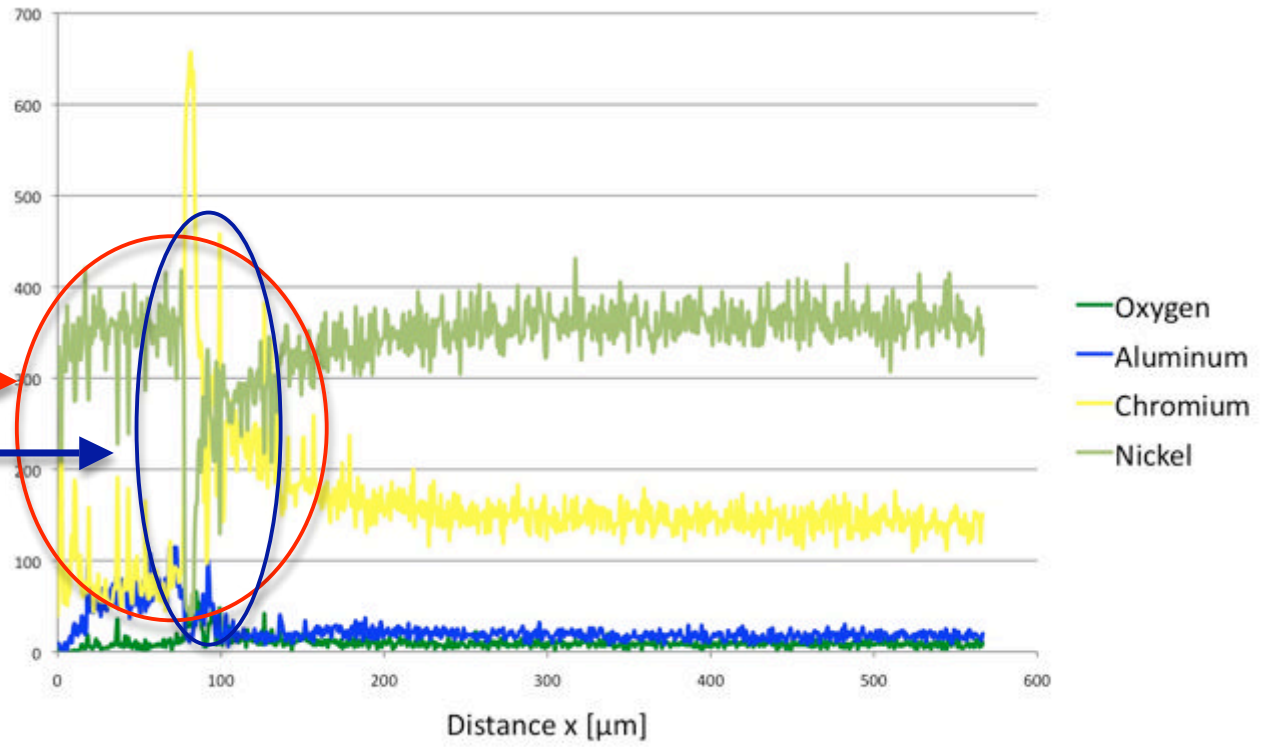

Graph 7: Displayed is the results of the EDAX line – scan to the left hand side. The nickel-oxide layer as well as the aluminum and chromium – oxide layer is clearly visible (area 1 – red circle). Furthermore the nickel depleted area, which is caused by the Kirkendall effect can be easily identified (area 2 – blue circle).

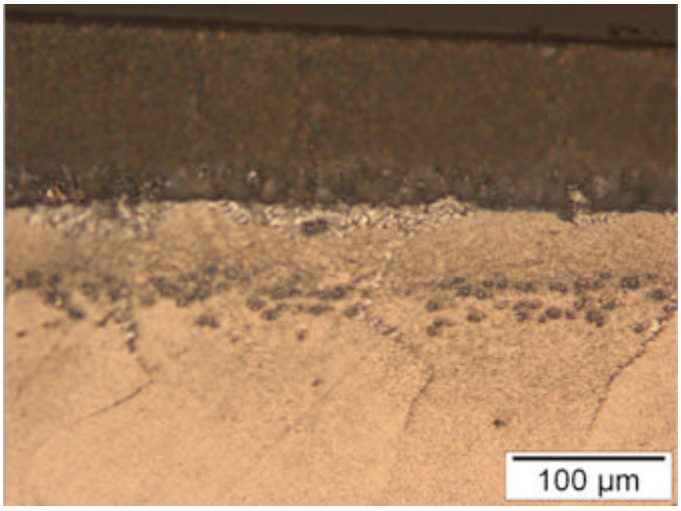

Figure 36: H214Al (750 C for 24 h) note the two different oxide layers as well as the Kirkendall effect.

While in H214 the Kirkendall effect was obviously easily defined to one element, it posed a challenge to determine in H214Al (Figure 36). Although on the elemental maps (Figure 37), the Kirkendall effect does occur, visible on Graph 8 and Figure 40. The oxide layer of H214Al is more complex than that of H214. There is already a high content of chromium in the first oxide layer. The chromium content is increasing, while nickel and aluminum are on a regional low (Graph 8). The bulk material of H214Al is affected to 200 µm below the surface (Graph 8).

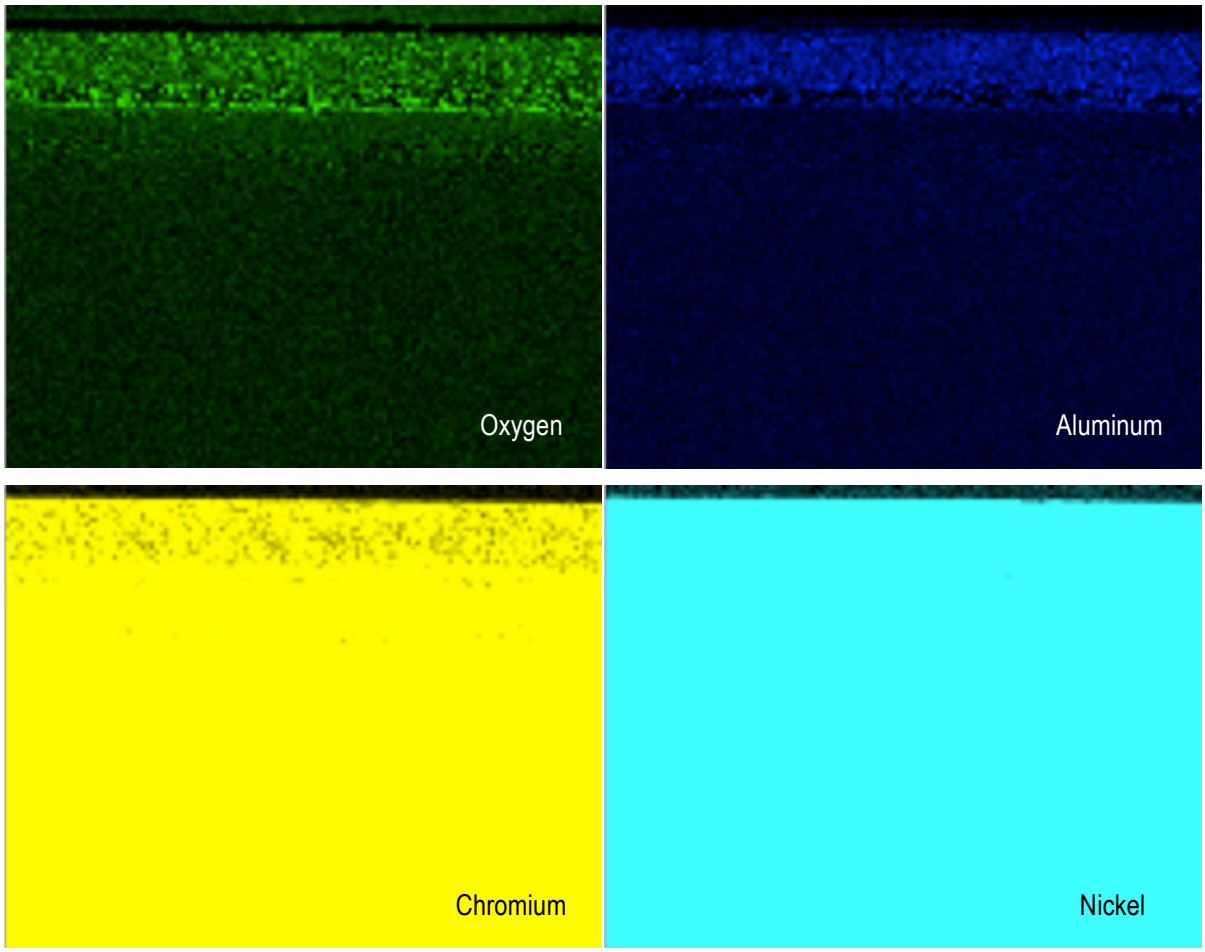

Figure 37: Element maps of H214Alnneled at 750 °C for 1000h. The oxide front, the aluminum oxide and the chromium layer are clearly visible. Nickel on the other hand seems not to be as severe affected as before.

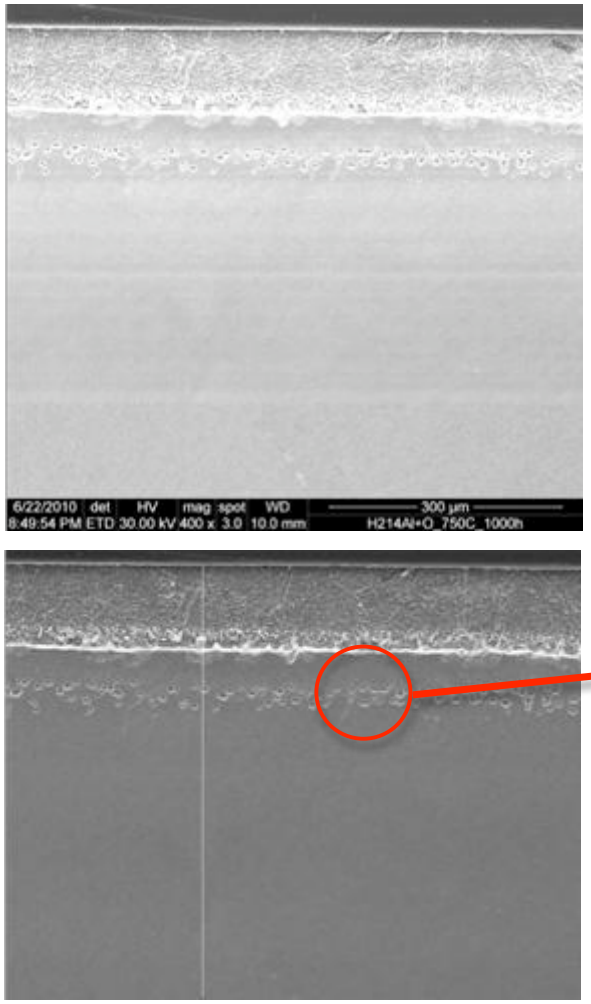

Figure 38: Line-scan of H214Al

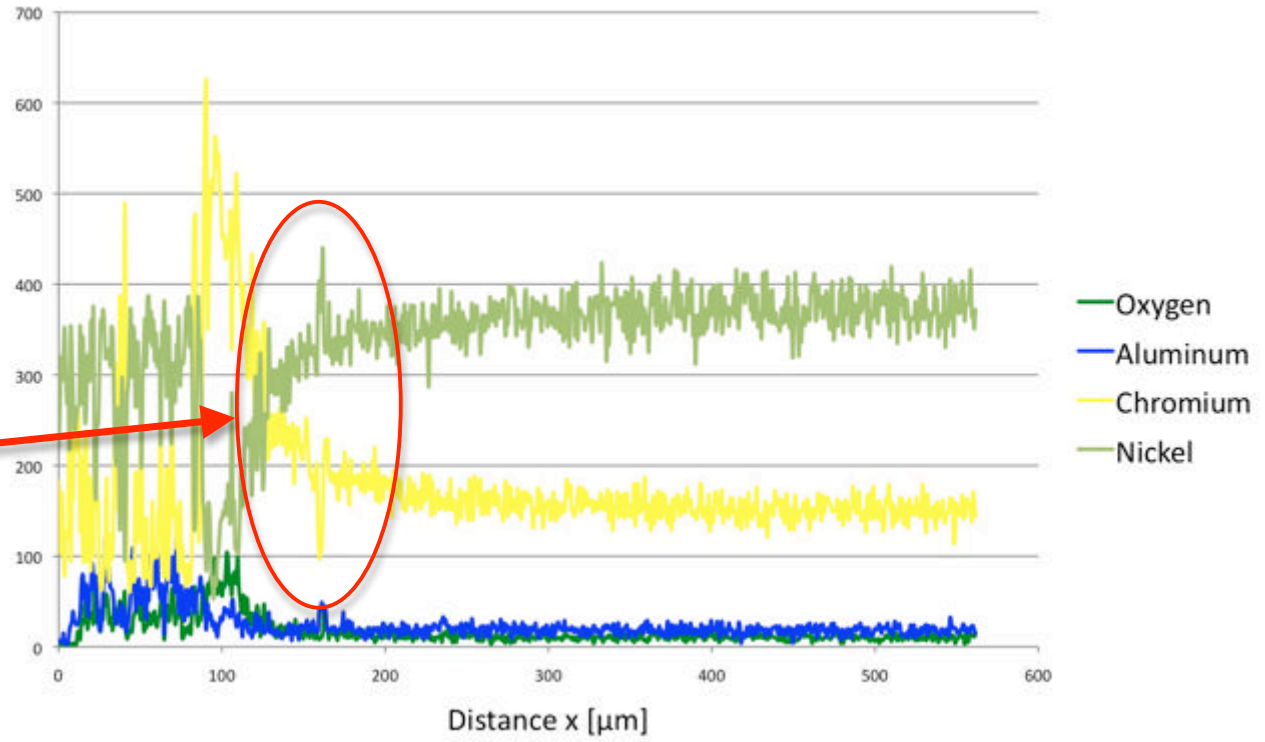

Graph 8: As seen earlier distinct patter of nickel, aluminum and chromium are visible. Apparently the Kirkendall is caused chromium and appears to be deeper inside the material compared to H214 (area1 – red circle).

4.2.3 H1560

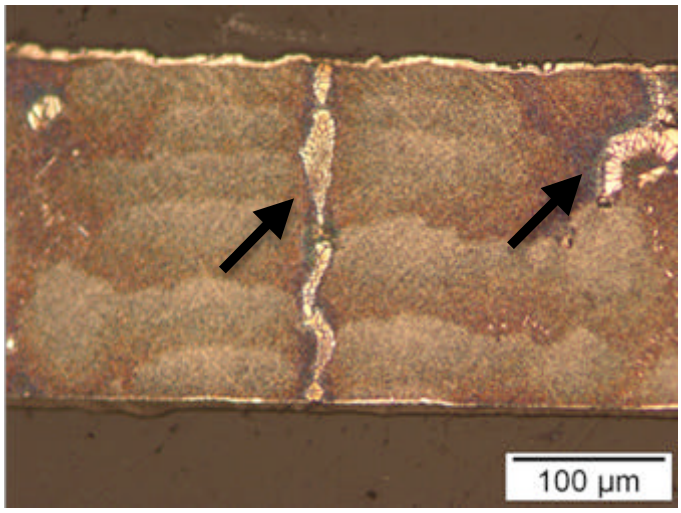

Figure 39: H1560 annealed at 1000 °C for 24 hours. Note the marked areas, which show the crystal growth of Ni_3Al.

Tests weren't limited to technical materials only; they included experimental materials such as H1560.

No effects could be observed on H1560 treated at 750 °C with Carbon for 1000h or at 750 °C for 24 hours at. The experiments conducted at 750 °C for 1000 hr (exposed to air) and at 1000 °C for 24 hr (exposed to carbon) showed interesting results.

H1560 is a nickel based single crystal with a high fraction of Ni_3Al. The volume fraction of Ni_3Al is thought to be 70 volume-percent, ensuring an optimal high creep behavior. The nickel-matrix and Ni_3Al precipitates are forming a coherent interface, which only allows similar diffusion properties, common in a bulk system. The reason being that the diffusion behavior is further dependent on the size of the mismatch of the interfaces. Consequently, a low diffusion rate for carbon was anticipated. Carbon diffuses alongside grain-boundaries first, before dissolving into the bulk material. Moreover, the high content of aluminum, which is necessary for a Ni_3Al-phase (which only occurs if 20 to 30% atom percent of aluminum is available in the system), supposedly hinders the diffusion of carbon. The simulations prove this by visualizing the carbon's avoidance of areas with a higher aluminum concentration.

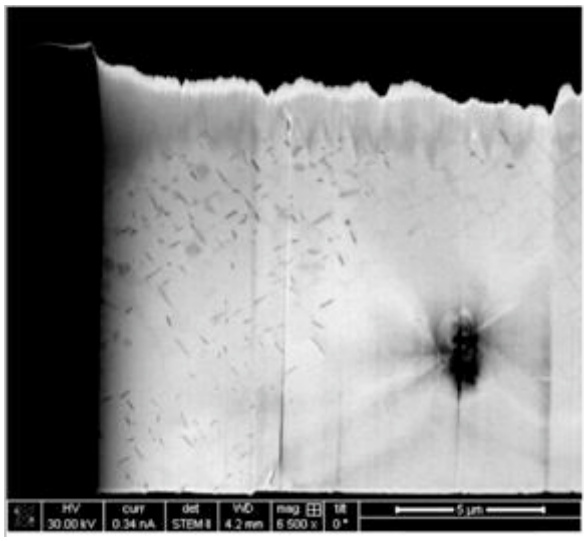

Figure 40: STEM foil of H1560 showing carbides and an area not affected by carbon.

Although, it was not possible to achieve reliable results using elemental mapping or an EDAX line scan, it was possible to see carbon particles by using the FIB in a STEM mode (Figure 40).

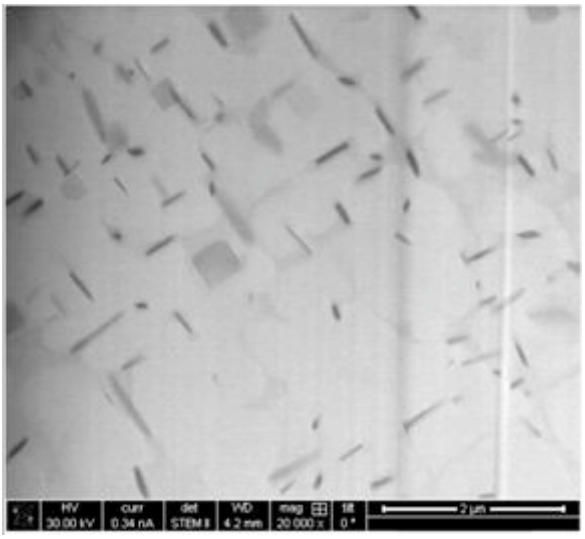

Figure 41: Carbon particles alongside the coherent interface of Ni and Ni_3Al in H1560.

In the first section of the STEM foil carbides are clearly visible (Figure 41). It appears that carbon is not affecting the Ni_3Al areas, instead trying to work its way around them. It diffuses alongside the Ni – matrix and the Ni_3Al phase, but not into the Ni_3Al phase. Diffusing alongside the coherent interfaces hinders carbon from dispensing faster into the bulk, which is the reason why the whole material is not as influenced by the carbon diffusion as H214 or H214Al. The high aluminum content might also hinder the advance of carbon in the material according to the simulation results.

The higher the concentrations of carbon, to which Ni_3Al is exposed to, the less ordered Ni_3Al appears. The carbon concentration is affecting the ordered interfaces starting to disarray and dissolve it. While a perfect order of Ni and Ni_3Al in a 001 - orientation is shown (Figure 42) in unaffected areas of the material, the more chaotic the material appears at higher carbon concentrations (Figure 40).

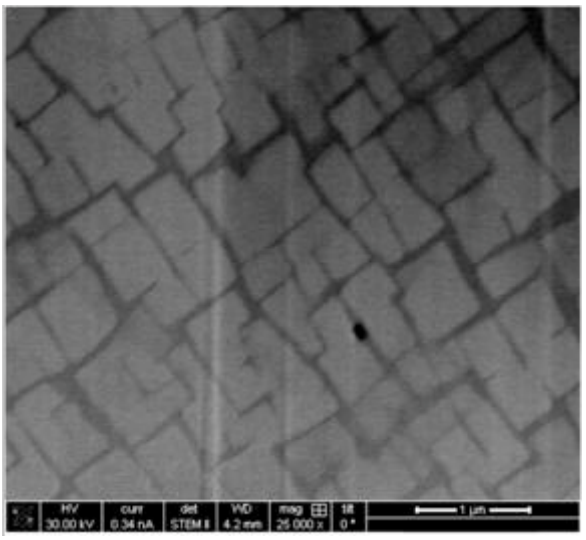

Figure 42: Ni and Ni_3Al interface in a perfect [100] plane, which is visible by the cubic order of the material.

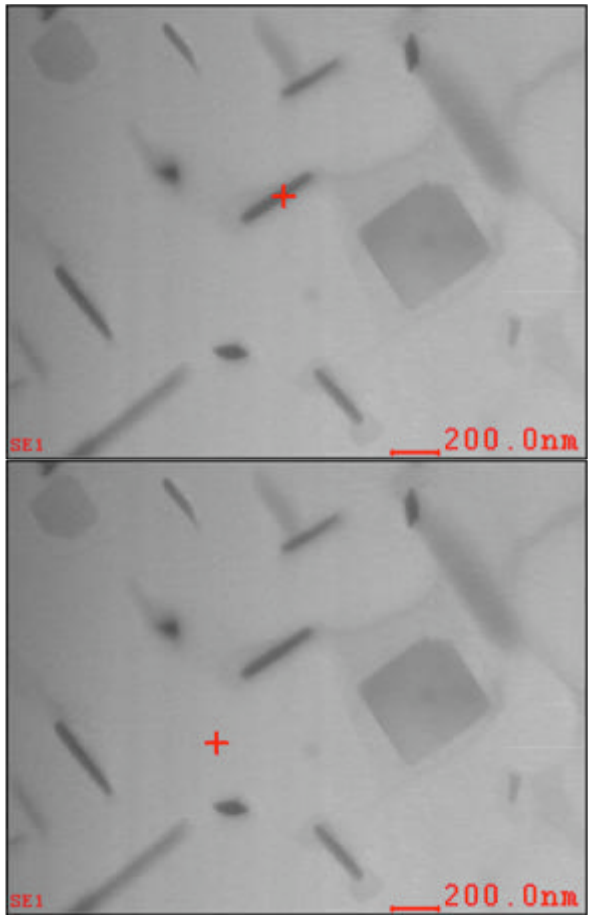

Figure 43: Characterization of a precipitate in H1560 and its matrix.

Table 5: Elemental characterization of a carbon affected area in H1560. Note below the weight and atom percentages retrieved form EDAX characterization.

Element	Wt%	At%
C	35,98	64,44
Al	6,74	5,39
Si	30,24	23,16
Cr	1,24	0,51
Ni	13,95	5,11
Ta	11,84	1,4

Element	Wt%	At%
C	39,25	65,16
Si	33,67	23,91
Cr	0,77	0,29
Ni	17,46	5,79

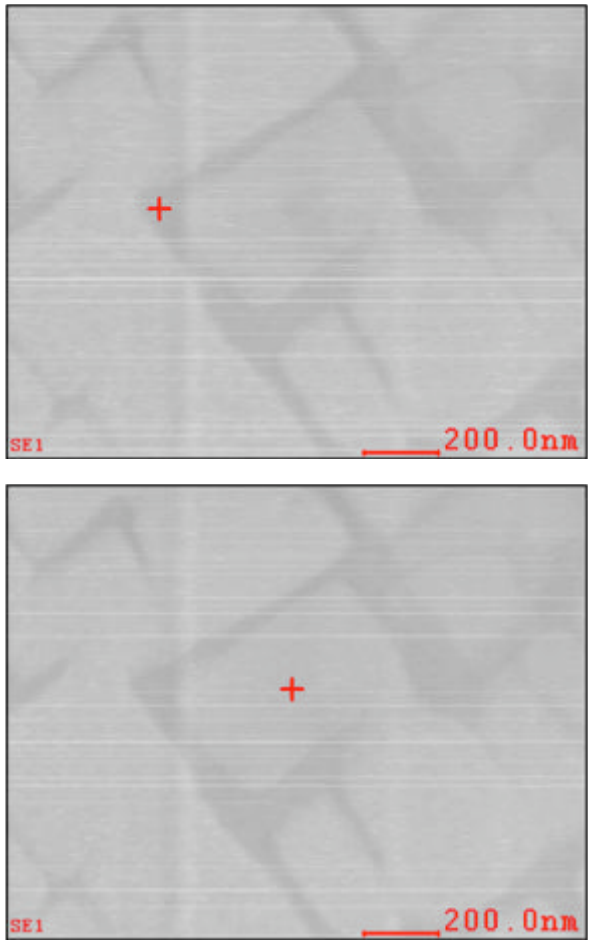

Figure 44: EDAX characterization of the unaffected zone in H1560

Table 6: Elemental characterization of a non - affected area in H1560. The Ni and Ni3Al phases and interfaces are clearly visible to the left hand side. The data was obtained by EDAX characterization.

Element	Wt%	At%
C	45,96	67,61
Al	7,55	4,94
Si	41,80	26,30
Cr	2,40	0,81
Ni	11,08	3,33

Element	Wt%	At%
C	39,94	65,86
Al	7,24	5,31
Si	39,59	27,92
Cr	1,15	0,44
Ni	11,18	0,38
Ta	0,9	0,09

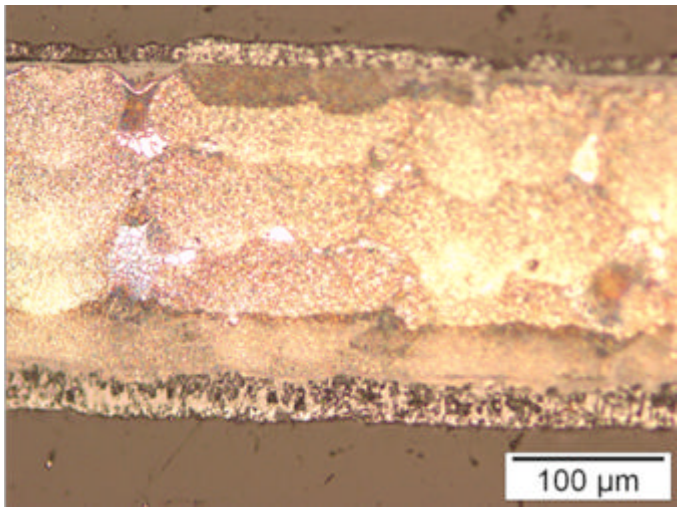

Figure 45: H1560 annealed at 750 °C for 1000 hours at air

Carbon seems to have a minor effect on the material during the testing period. Oxygen on the other hand has a similar effect on the material as on the other materials at a testing time of 1000 hours at 750 °C (Figure 45). Similar to previous samples exposed to air, the sample showed a huge affected area with a wide spread diffusion front. It is even more distinct than in other materials (Figure 46). The advancing nickel and its depleted plus the aluminum and chromium rich areas zone are clearly visible. The depth of the affected zone can also be seen by a line-scan (Figure 47).

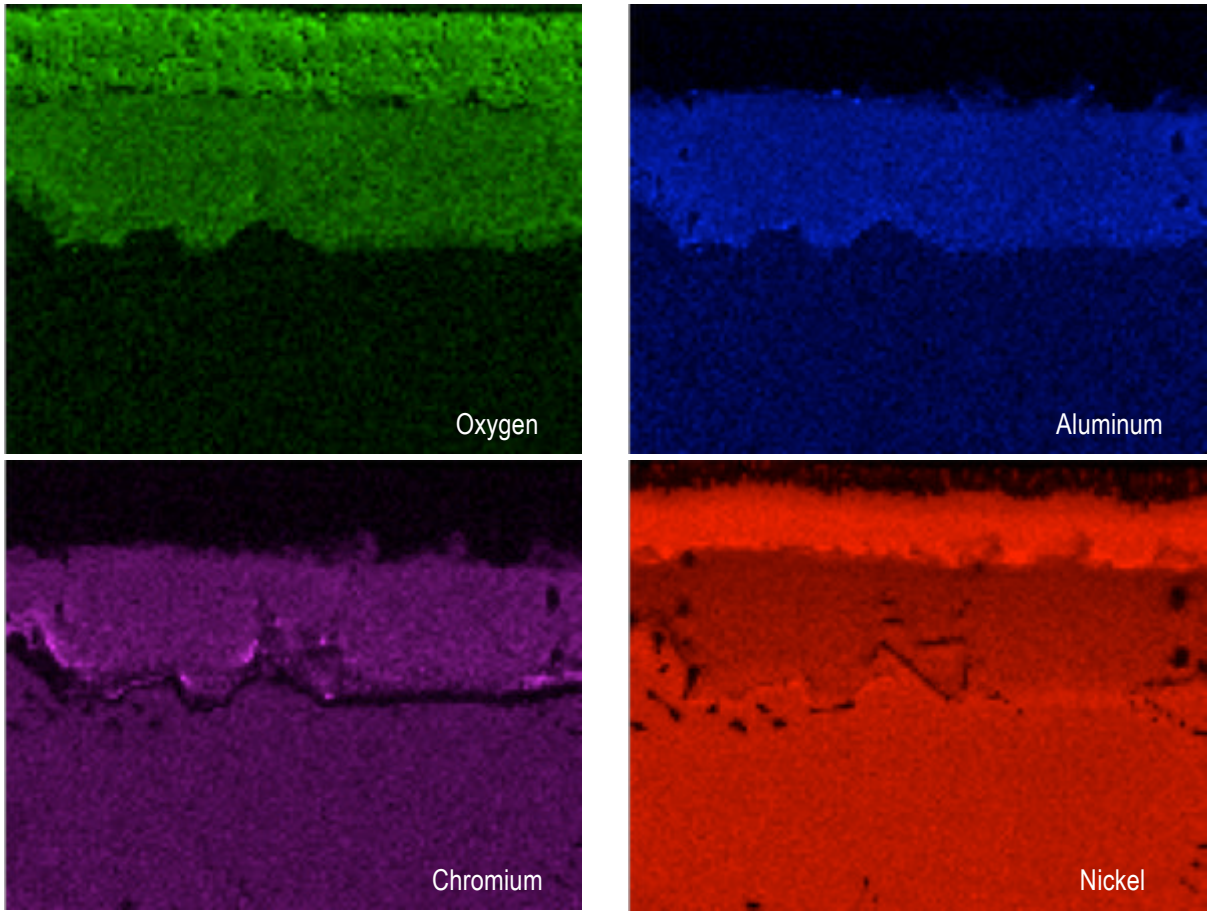

Figure 46: Element map of H1560 ordered as followed; Oxygen, Aluminum, Chromium and Nickel. The oxidation front is clearly visible as well as the broad areas of aluminum and chromium oxides.1

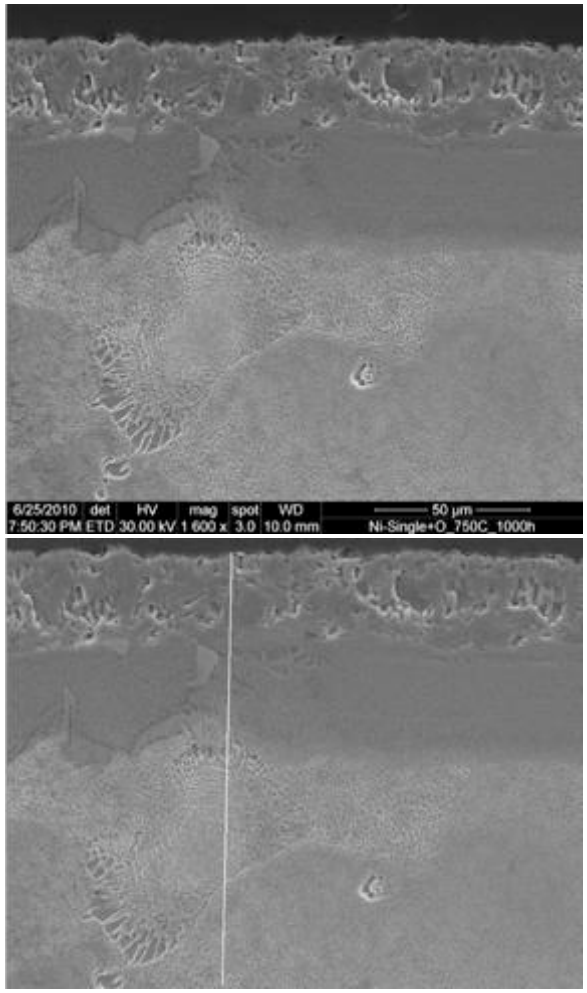

Figure 47: Line-scan of H1560 heat-treated at 750 °C for 24 hours at air.

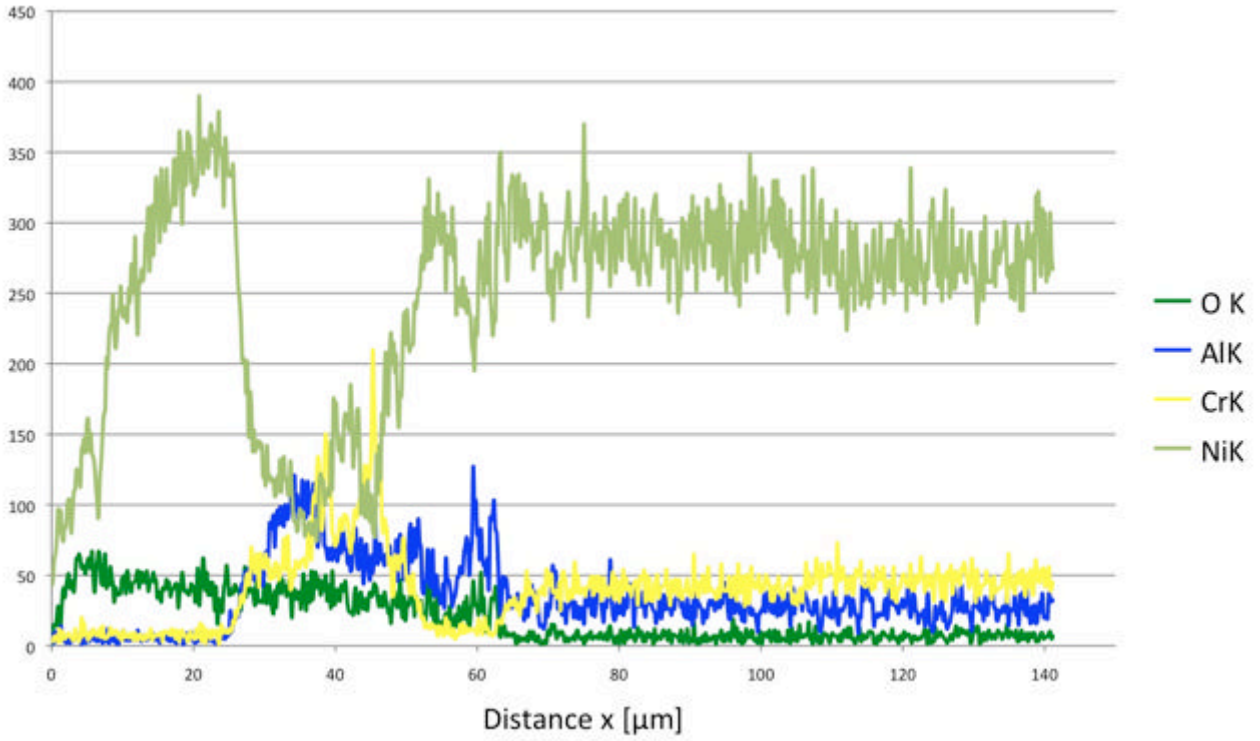

Graph 9: The characteristics of the two oxide layers are clearly visible in. In the first 20 µm a porous nickel oxide layer is located; the second, denser aluminum and chromium oxide layer starting at around 25 µm. The material is affected to a depth of at least 80µm by the diffusion of oxygen into the system. This is - compared to the other materials - rather shallow, which is quite well. As observed before, oxygen diffused to a depth of around 150 µm.

The oxide layers were characterized using FIB in STEM mode, to achieve a precise data collection. The material for the STEM foil was cut from an area with a predefined oxidation layer (Figure 48). To avoid damage to the sample, its surface was coated with carbon. To delineate it, an ion beam was used afterwards.

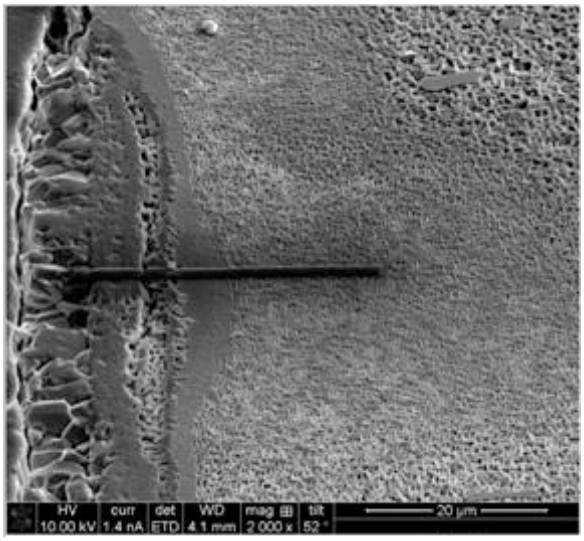

Figure 48: Area of H1560 preparation before cutting out the STEM foil.

The different areas one to four were later characterized with the energy dispersive X-ray diffraction (Figure 49). There are 4 main stages of oxidation visible starting from the bulk material to the surface (right to left). While the first stage shows no influence of oxygen and displays a ordered Ni-matrix and Ni_3Al bulk system, stage 2 displays already first signs of oxidation (Figure 50). The Ni_3Al phases are dissolving, yet are still recognizable. Afterwards the phase is unrecognizable from the rest of the matrix. This results from the fast diffusion of nickel towards the surface and the high affinity of aluminum toward oxygen forming Al_2O_3. Further reasons are: the high affinity of chromium forming Cr_2O_3 and therefore together with aluminum forming the first oxide layer (Figure 51).

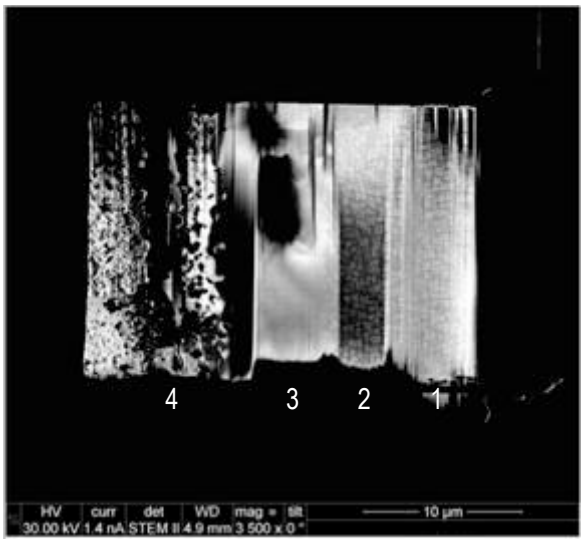

Figure 49: STEM foil of H1560 displaying different stages f oxidation.

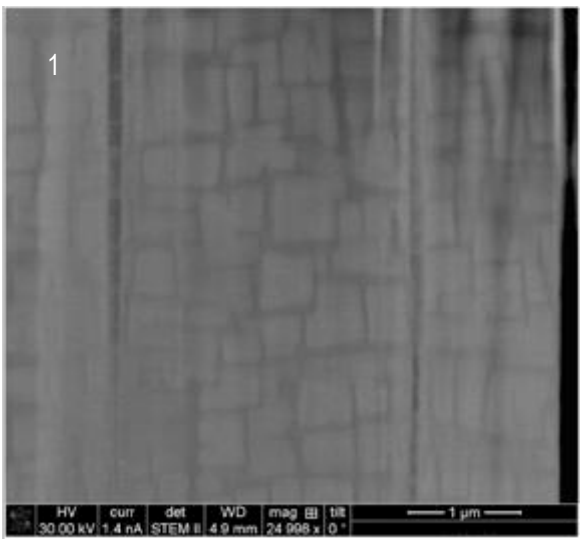

Figure 50: Area 1 of H1560 is not affected by oxidation.

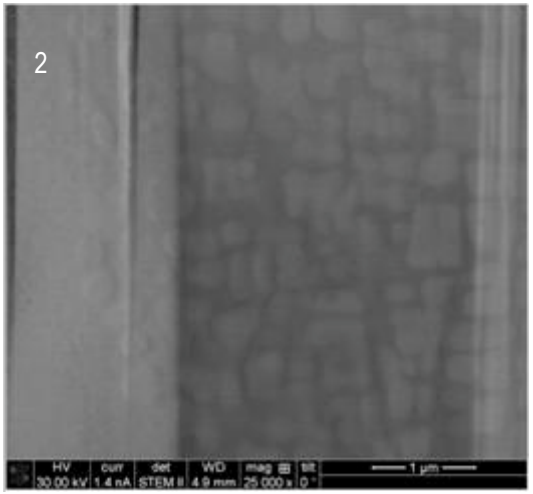

Figure 51: Area 2 is showing the first effects of oxidation in H1560.

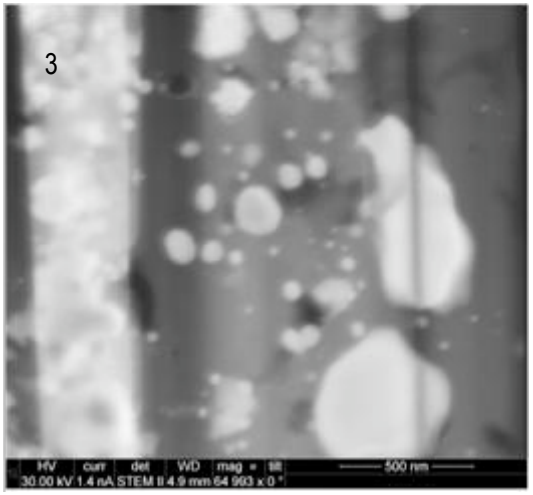

Figure 52: Major changes of the microstructure due to oxidation can be observed in area 3.

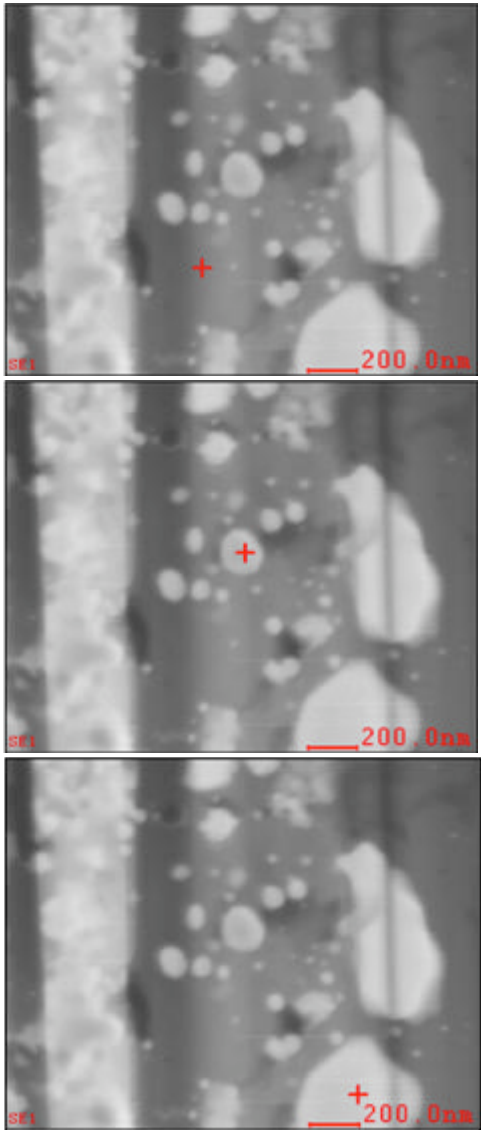

Figure 53; EDAX characterization of area 3, which displays the most severe changes in microstructure due to oxidation.

Table 7: Chemical composition of specific locations in area 3 shown to the left.

Element	Wt%	At%
O	71,57	81,88
Ni	02,42	00,76
Al	23,99	16,27
Si	01,23	00,81
Cr	00,79	00,28

Element	Wt%	At%
O	51,90	65,33
Al	45,06	33,63
Ni	3,03	1,04

Element	Wt%	At%
O	15,84	32,63
Al	30,45	37,21
Ni	53,71	30,17

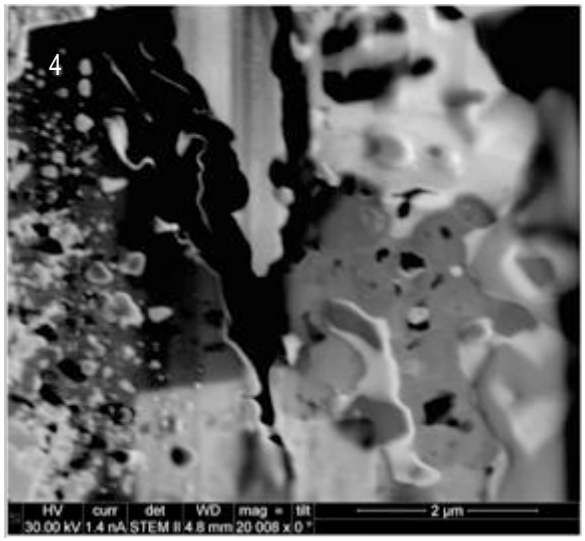

Figure 54; Area 4 of H1560 affected by oxidation.

The second oxide layer or the last stage is a nickel – oxygen layer (Figure 54). This layer has already suffered severe damage due to oxidation and appears porous, when examined via FIB in STEM mode.

5. Discussion

In order to verify our methods and improve our results, we compared our calculations to those conducted already during the research of Y. Mishin et al. [4]. We also constructed a Ni_3Al 2x2x2 super cell and created a Ni in one and an Al vacancy in a system.
The compared results (Graph 10) had only a small mismatch. The difference in the results can be explained by the use of

(i) different pseudo-potentials (we used PAW-PBE)
(ii) different k-point grid
(iii) different E-cut

Unfortunately, those values were not given in the paper and could not be reevaluated. Therefore, we considered our calculations as accurate and continued our research.

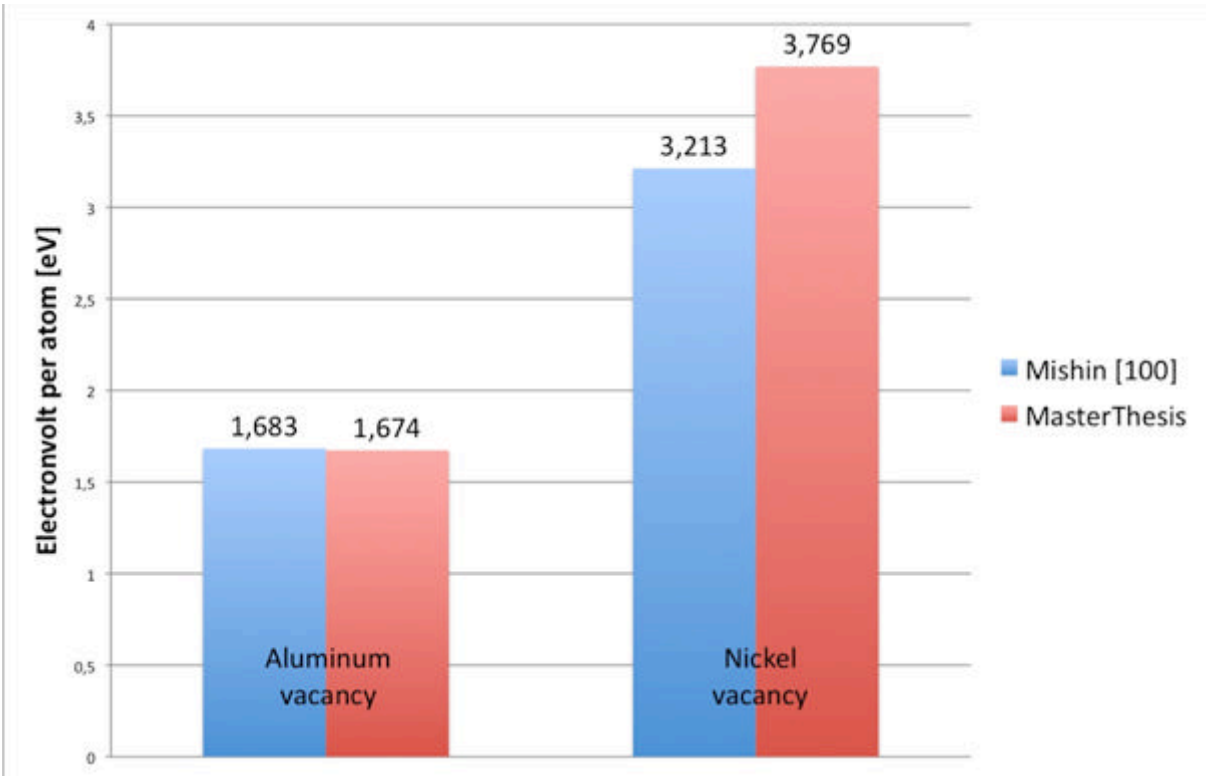

Graph 10: Comparison of the simulation approach with previous studies, here a study conducted by Mishin on the point defect formation energy in a pour Ni_3Al system by creating a Ni and an Al vacancy.

The aim of this thesis was to fully comprehend the behavior of interstitial elements in Nickel super alloys focused on aluminum rich areas, which are important for the development of Ni_3Al. Ni_3Al is responsible for the high temperature creep resistance. Therefore three materials were selected H214, H214Al and H1560. To achieve valuable results using VASP simulation program we decided to use a 3x3x3 unit cell with 108 atoms. The interstitial element was simulated by adding one atom of a specific kind.

The carburization tests were conducted in vacuum, which leaves room for improvement by adding an inert gas into the quartz-tube. The inert gas is going to alter the gas pressure, which might lead to a different type of carburization.

The simulation results obtained, suggest a dislike of carbon towards aluminum. Henceforth, carbon is going to avoid aluminum-rich areas, opting instead for a nickel-rich matrix. Oxygen has a high affinity for aluminum atoms in comparison. Those results were helpful in understanding why certain areas were affected by carburization, while others remained unharmed and evaluate the deep impact of oxygen. The high affinity of nickel towards oxygen and the ability of nickel to diffuse faster to the surface than it is able to diffuse inside the bulk material, results in a dense nickel-oxide on the surface aside of a nickel depleted areas inside the material itself. This behavior leads to the observed Kirkendall effect. However, the simulation is of limited use due to the small-sized system, which can be simulated. The results may only be accurate in bulk systems and coherent interfaces, while being relatively unimportant in terms of materials with grain-boundaries with a large mismatch. Other materials than nickel and aluminum weren't taken into account due to the limitation on the system size. Yet, graphic evidence from the experiments show that chromium plays an important role in the diffusion of carbon by forming $Cr_{23}C_6$ at the grain-boundaries and forming a Cr_2O_3 layer.

In certain ways, the simulation allowed to almost unerringly predict the behavior in the materials before even conducting the experiments. As calculated beforehand during the simulations, carbon does require a high amount of energy in order to be placed in an aluminum rich area. While in H214 carbon not only formed $Cr_{23}C_6$ at the grain boundaries, it also diffused into the grain itself. H214Al on the other hand, with a twice as high aluminum content as H214, was not affected by carbon as severely as H214. $Cr_{23}C_6$ formed alongside the grain boundaries, while carbon had not yet affected the grain itself completely. H1560, with its well-ordered microstructure, forced carbon to diffuse alongside the coherent Ni-Ni_3Al interfaces into the bulk material. The inability to use large mismatches of the grain

boundaries, caused carbon was forced to diffuse alongside high aluminum rich areas, which slowed down its diffusion process dramatically. Therefore, no carburization effects could be observed with optical microscope, SEM or EDAX. Using STEM, it was possible to find traces of carbon alongside Ni_3Al in the nickel bulk, howbeit the Ni_3Al phase itself was not influenced.

The simulation results predicted the behavior of oxygen well, but failed to predict the behavior of nickel and chromium. Although it was obvious, that the energy necessary to introduce an oxygen atom into a system was far less than for carbon, the impact oxygen had on the material was surprising. Nickel diffused to the surface leaving gaps in the microstructure, which could not be filled by following nickel atoms due to their lower diffusion coefficient and forming a Kirkendall effect. It formed a thick NiO layer on the surface of the material, which slowed down the diffusion of oxygen into the bulk. As soon as oxygen passed the first oxide layer it formed due to its high affinity to aluminum and chromium, a second denser oxide layer of Al_2O_3 and Cr_2O_3 established. The high affinity toward aluminum was predicted by the simulation results; the importance of chromium due to limitations of the system size was not anticipated however.

The simulations were conducted using a pure nickel and a nickel aluminum system. The amount of used elements was restricted by the simulation code itself, due to the fact that the computational requirements would have been too high. The point defect formation energies were calculated using only one interstitial atom in the system and therefore could not predict the behavior of other interstitial elements close to each other.

Carbide formations were observed in several samples, which could not be predicted by the simulation results. They would have been of high significance concerning the possible forming of carbides at grain boundaries reducing the mechanical strength and corrosion resistance of a material. Therefore, the riddle to solve: at which distance the interstitial elements can “feel” each other, and if they are drawn together (as could be observed by carbon) are they going to repel each other. As mentioned before, the simulation results are predicting a diffusion or possible location trend of carbon and oxygen, but this is only correct for very specific materials as H1560 or very specific areas inside certain materials. In order to describe the interstitial element behavior in technical materials such as H214, more information has to be implemented in the simulation.

6. Future Prospects

To improve the method for predicting the behavior of interstitial elements in technical materials, several more methods could be implemented. To achieve a better simulation of the technical material, the problematic factors have to be located first.

With the current codes available, it is not advisable to calculate systems with more than two main elements. Therefore several systems have to be created in which several steps of the reaction inside the material can be simulated.

The interaction of interstitial elements toward each other should be taken into account as in order to predict their behavior (e.g. forming of carbides).

Transition state theory - the calculation of transitions like the diffusion in solids - must be conducted to allocate possible pathways.

For the transition state theory two basic assumptions have to be made:

(i) The rate is slow enough that Boltzmann statistics is applicable for the initial state and
(ii) an energy divide (a n-1 dimensional energy surface, where n is the number of degrees of freedom) can be identified such that the reaction trajectory crosses only once.

To determine the activation barriers and saddle points for the diffusion between octahedral and tetrahedral interstitial sites the use of the so-called nudged-elastic band method (NEB-method) is advisable (Figure 55).

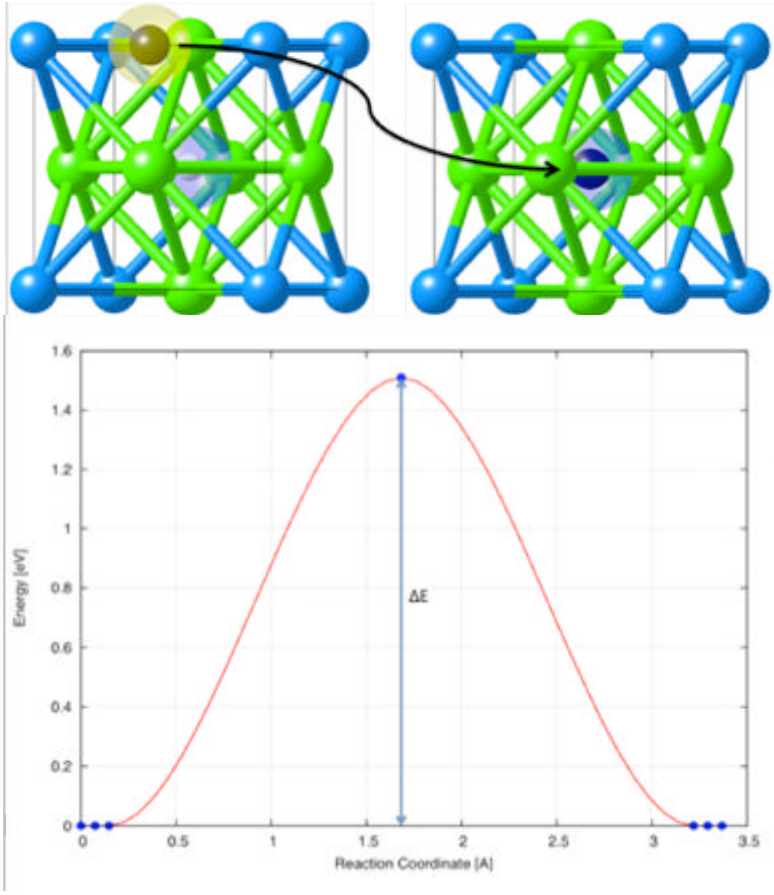

Figure 55: Migration of C – Atom at an octahedral site for a unit cell of Ni_3Al. ΔE is the energetic barrier (saddle point), which the atom has to overcome in order to migrate to the next possible position.

The thus acquired simulation results allow to adept a program code for Kinetic Monte Carlo using the Harmonic Transition State Theory (HTST). This is a method for simulating the dynamics of a rare event system like diffusion in solids. HTST is often referred to as the Vineyard theory [50]. In order to simulate rare events like diffusion, the migration energy barriers have to be overcome in order to migrate from position 1 to position 2 (Figure 55). Transition pathways are defined the saddle point on the potential energy surface. The saddle plane is defined as the dividing surface. It is further assumed that the potential energy near the basin minimum is well described and that the same applies for the forms perpendicular to the reaction coordinate at the saddle point [50].

$$k^{HTST} = \frac{\prod_{i}^{3N} \nu_i^{\min}}{\prod_{i}^{3N-1} \nu_i^{sad}} \exp\left(\frac{-E_{static}}{k_B T}\right)$$

E_{static} is the migration barrier height and k_B is the Bolzmann constant. In the prexponential factor, $\{\nu_i^{min}\}$ are the 3N normal mode frequencies at the saddle and so forth. K^{HTST} only requires information about the minimum and the saddle point for a given pathway. The HTST tends to be very accurate within 10-20%, up to at least half the melting point for diffusion events in most solid materials ([51, 52]). Since prefactors are often in the range of $10^{12}s^{-1}$ – $10^{13}s^{-1}$, a common approach is to choose a fixed value in this range to limit the time spent on computing the normal modes for every saddle point [53].

Using those combined methods it should be possible to approximate the simulation of a technical material.

A new approached was developed and is not as known as KMC is the *modified embedded-atom* method or MEAM. Unfortunately, it hasn't been commonly exploited, hence only a few pseudo-potentials are available for usage.

7. Literature:

1. H. K. D. H. Bhadeshia, Nickel Based Superalloys, www.msm.cam.ac.uk/ phase-trans/2003/Superalloys/superalloys.html (accessed on March 15, 2009)
2. Madeleine Durand-Charre, The Microstructure of Superalloys ISBN: 90-5699-097-7
3. Y. Mishin, Acta Mater 2004; 52: 1451-1467
4. Y. Mishin, A.Y. Lozovoi, A. Alavi, Physical Review 2003; B67: 014201
5. Hohenberg, P. and Kohn, W. Phys. Rev. 1964, Vol. B136, p. 864
6. Kohn, W. and Sham, L. Phys. Rev. B. 1996, Vol.54, p. 11169
7. MedeA User Guide S.174
8. Janak J.F., Phys. Rev. Lett. 1980, Vol.45, p 566
9. Schulte F.K., Z. Phys. 1977, Vol. B27, p. 303
10. von Barth J., and Hedin L., J. Phys. C. 1972, Vol. C5, p.1629
11. Gunnarson O. I., Lundquist B and Lundquist S., Solid State Communications. 1972 Vol. 11, p. 149
12. Becke A.D., Density-functional exchange-energy appromixmation with correct asymptotic behaviour. Phys. Rev. A. 1988, Vol. 38, pp. 3098-3100
13. Perdew J.B. and Wang Y., Phys. Rev. 1992, Vol. B45, p. 13244
14. Koelling D.D. and Harmon B.N., J. Phys. C. 1977, Vol. C 10, p. 3107
15. http://en.wikipedia.org/wiki/Brillouin_zone
16. http://www.iue.tuwien.ac.at/phd/hackel/_3462_figure895.gif
17. http://en.wikipedia.org/wiki/Pseudopotential
18. Nickel Alloys, ISBN: 0-8247-0440-1 S. 145-155
19. Introduction to the High-Temperature Oxidation of Metals, ISBN: 978-0-521-48042-0, S.272
20. Y. Mishin, Acta Mater. **52**, 1451 2004
21. Amouyal, Mao, Seidman, Segregation of tungsten in a Ni-based superalloy
22. Fu CL, Painter GS. Acta Mater 1997; 45:481
23. Arthur F. Voter, K.E. Sichafus et al (eds.), Radiation Effects in Solids, 1-23, Springer 2006
24. G. Kresse and J. Furthmuller, Comput. Mater. Sci. 6, 15 (1996)
25. G. Kresse and J. Hafner Phys. Rev. B 49, 14251 (1994)
26. R. C. Reed, The Superalloys: Fundamentals and Applications (Cambridge University Press, New York, 2006), p. 372
27. MedeA User Guide S. 182
28. http://cms.mpi.univie.ac.at/vasp/vasp/vasp.html

29. LG Wang, CY Wang, Effect of boron and sulphur on the electronic structure of grain boundaries in Ni . Computational Materials Science (1998) vol. 11 pp. 261-269
30. BH Sencer, GM Bond, FA Garner, ML Hamilton, SA Maloy, WF Sommer et al. Correlation of radiation-induced changes in mechanical properties and microstructural development of Alloy 718 irradiated with mixed spectra of high-energy protons and spallation neutrons . Journal of Nuclear Materials (2001) vol. 296 pp. 145-154
31. T Jeske, M Seibt, G Schmitz et al. Microstructural influence on the early stages of interreaction of Al/Ni-investigated by TAP and HREM. Materials Science and Engineering (2003) vol. A353 pp. 105-111
32. Yaron Amouyal, Zugang Mao, David N Seidman, Segregation of tungsten at γ[sup ′](L1[sub 2])/γ(fcc) interfaces in a Ni-based superalloy: An atom-probe tomographic and first-principles study. Appl. Phys. Lett. (2008) vol. 93 (20) pp. 201905
33. G Kresse, J Furthmiller Efficiency of ab-initio total energy calculations for metals and semiconductors using a plane-wave basis set . Computational Materials Science (1996) vol. 6 pp. 15-50
34. Emmanuel Cadel Cristelle Pareige Bernard Deconihout Pierre Caron Didier Blavette, Phase Transformation and Segregation to Lattice Defects in Ni-Base Superalloys. Microscopy and Microanalysis (2007) vol. 13 pp. 464-483
35. JK Heuer, PR Okamoto, NQ Lam, JF Stubbins, Disorder-induced melting in nickel: implication to intergranular sulfur embrittlement . Journal of Nuclear Materials (2002) vol. 301 pp. 129-141
36. M Kalay, H H Kart, S Ã–zdemir Kart, Elastic properties and pressure induced transitions of ZnO polymorphs from first-principle calculations. Journal of Alloys and Compounds (2009) pp. 1-8
37. H H Kart, M Uludogan, T Cagin, DFT studies of sulfur induced stress corrosion cracking in nickel. Computational Materials Science (2009) vol. 44 (4) pp. 1236-1242
38. L Kovarik, R R Unocic, Ju Li, P Sarosi, C Shen, Y Wang, M J Mills, Microtwinning and other shearing mechanisms at intermediate temperatures in Ni-based superalloys. JOURNAL OF PROGRESS IN MATERIALS SCIENCE (2009) pp. 1-35
39. KYCheng, DHKim, YSYoo, CYJo, TJin, ZQHu, Microstructural Stability of a Single Crystal Superalloy DD8 during Thermal Exposure. J. Mater. Sci. Technol. (2008) vol. 24 pp. 1-4

40. Petr Lazar, Raimund Podloucky, Ductility and magnetism: An ab-initio study of NiAl-Fe and NiAl-Mn alloys. Intermetallics (2009) vol. 17 (9) pp. 675-679
41. Saito and Harada. The Monte Carlo simulation of ordering kinetics in Ni-base superalloys . Materials Science and Engineering (1997) vol. A223 pp. 1-9
42. Wagner and Windl. Lattice stability, elastic constants and macroscopic moduli of NiTi martensites from first principles. Acta Materialia (2008) vol. 56 (20) pp. 6232-6245
43. Wang and Wang. Desity functional theory study of Ni/Ni3Al interface alloying with Re and Ru. Surface Science (2008) vol. 602 pp. 2604-2609
44. Wang and Wang. Influence of the alloying element Re on the ideal tensile and shear strength of γ′-Ni3Al. Scripta Materialia (2009) vol. 61 (2) pp. 197-200
45. Yang et al. The kinetics of two-stage formation of TiAl3 in multilayered Ti/Al foils prepared by accumulative roll bonding. Intermetallics (2009) vol. 17 (9) pp. 727-732
46. Cong Wang, Chong-Yu Wang. Ni/Ni3Al interface: A density functional theory study . Applied Surface Science (2009) vol. 255 pp. 3669-3675
47. Nickel Alloys, ISBN: 0-8247-0440-1 S. 145-155
48. Phase transformation in metals and alloys ISBN: 978-1-4200-6210-6(0)
49. J. F. NYE, Physikal Properties of crystals ISBN 978-0-19-851165-6
50. Arthur F. Voter, Introduction to the Kinetic Monte Carlo Method
51. R. Norris, Markov Chains (Cambridge University Press, Cambridge, UK, 1997).
52. W. Feller, An Introduction to Probability Theory and its Applications, Vol. 1,
53. Wiley, New York (1966). 22. D.T. Gillespie, J. Comp. Phys. 22, 403 (1976).

8. Appendix

Table-A 1: The structure and the buildup of a 4x4x4 super-cell is shown. In this case, it is a 4x4x4 Ni super-cell, which is easier to display than a more complicated super-cell with single point defect.

4x4x4 Ni-Super cell

Header for identification of the cell	(Ni)256 (P1) ~ Ni Super cell (VASP)		
Coordinates for the unit cell	x – Axe	y - Axe	z - Axe
	1.0		
	7.0467	0.0000	0.0000
	0.0000	7.0467	0.0000
	0.0000	0.0000	7.0467
Number of atoms in the system	256		
	x - Axe	y - Axe	z - Axe
Coordinates of each atom inside the super cell. Only the first coordinates are shown due to the fact that there are 256 positions.	Direct		
	0.0000	0.0000	0.0000
	0.0000	0.2500	0.2500
	0.2500	0.0000	0.2500

Table-A 1 and Table-A 2 are providing greater insight into the structure of a POSCAR or position file. The arrangement of the atoms is now visible and explained, therefore easy to reproduce (or they can be used as a sample to create new POSCAR-files for future studies).

Table-A 2: The structure 4x4x4 Ni3Al super-cell is shown. While most of the structure remains constant, the number of atoms for Ni changes due to the fact the system now has to accompany Al atoms as well. Therefore, the system contains 192 Ni atoms and 64 Al atoms. Analog to the POTCAR, the Ni atoms are arranged first, while the Al atoms are last in the row. This is important due to the fact that the order in the POTCAR and POSCAR file needs to be constant, otherwise a Ni pseudo-potential might be assigned to an Al atom.

4x4x4 Ni_3Al-Supercell

Header for identification of the cell	((Ni3 Al)64 (P1) ~ Ni3Al_1 (VASP)		
Coordinates for the unit cell	1.0		
	7.0467	0.0000	0.0000
	0.0000	7.0467	0.0000
	0.0000	0.0000	7.0467
Number of atoms in the system; here 192 Ni and 64 Al atoms	192	64	
Coordinates of each atom inside the super cell.	Direct		
	0.0000	0.0000	0.0000
	0.0000	0.2500	0.2500

Table-A 3 shows the structure of an INCAR file as well as key features, which are subsequently defined in the calculations conducted by VASP. An INCAR file, which was used for the calculations of the bulk system, ‘acts’ as display. The commands are explained below, so that calculations are easily duplicated if necessary.

As explained earlier in this thesis, the INCAR file is the main operational file, which has to be adjusted for each computer-system and each super cell. This can be rather difficult to receive.

Table-A 3: Structure of an operational INCAR file. Note that all commands and shortcuts are explained below due to simplicity. It is also possible to read them on the VASP homepage of the university of Vienna.

INCAR FOR Ni_3Al

SYSTEM = (Ni3 Al)8 (P1) ~ Ni3Al_1 (VASP)

PREC =	Accurate
ENCUT =	550
IBRION =	2
NSW =	100
ISIF =	3
ALGO =	Normal (blocked Davidson)
NELM =	60
NELMIN =	2
EDIFF =	1.0e-0.5
EDIFFG =	-0.001
VOSKOWN =	1
NBLOCK =	1
ISPIN =	1
INIWAV =	1
ISTART =	0
ICHARG =	2
LWAVE =	.FALSE.
LCHARG =	.FALSE.
ADDGRID =	.FALSE.
ISMEAR =	1
SIGMA =	0.2
LREAL =	.TRUE.
RWIGS =	1.15 1.18

PREC determines the energy cutoff ENCUT, if no value is given for ENCUT in the INCAR file [28].

ENCUT is the cut cut-off energy for plane waves in eV. All plane-waves with a kinetic energy smaller than E_{CUT} are included in the basis set

$$|G + k| < G_{cut} \quad with \quad E_{cut} = \frac{\hbar^2}{2m} G_{cut}^2$$

The number of plane waves differs for each k-point, leading to a superior behavior for e.g. energy-volume calculations [28].

IBRION determines how the ions are updated and moved [28].

NSW defines the numbers of ionic steps [28].

ISIF determines whenever the stress tensor is calculated and therefore controls which degrees of freedom (ions, cell shape, cell volume) are allowed to change [28].

ALGO defines which algorithm is used for the calculations (normal, very fast, fast, all, damped) [28].

NELM, NELMIN gives the max or the minimal number of iteration steps which should be performed [28].

EDIFF defines the breaking condition when **NELM** should be stopped [28].

EDIFFG defines as **EDIFF** the breaking condition for the iteration loop, only for the ionic relaxation loop [28].

If **VOSKOWN** equals 0, VASP uses the standard interpolation for the correlation part of the exchange correlation functional. If **VOSKOWN** is set to 1 the interpolation formula according to Vosko Wilk and Nusair is used, which enhances the magnetic moments and the magnetic energies [28].

NBLOCK controls how often the kinetic energy is scaled [28].

ISPIN is important for spin polarized or pin non-polarized calculations. INSPIN = 1 is for non-spin polarized while ISPIN=2 is used for spin polarized calculations [28].

INIWAVE is only used for start jobs [28].

ISTART determines if a WAVECAR file should be read or not [28].

ICHARGE determines how to construct the 'initial' charge density [28].

LWAVE determine if the wave functions, the charge densities are written or not [28].

ISMEAR determines how the partial occupancies are set for each wave function [28].

SIGMA determines the width of the smearing in eV [28].

LREAL determines whether the projection operators are evaluated in real-space or in reciprocal space. In reciprocal space the number of operations scales with the size of the basis set. In real space the projection-operators are confined to spheres around each atom. Therefore the number of operations does not increase with the system size but the projection operators must be optimized [28].

RIWGS stands for the Wigner Seitz radius and is optional [28].

Table-A 4 and Table-A 5 display the energy convergence of the free formation energy relative to the Energy Cut off and K-Point grid. The convergence of the lattice parameter is of great importance since the calculation time necessary to solve a problem is drastically reduced and the accuracy of the result is increased.

Table-A 4: Free formation energy convergence relative to the K-Points gird of a 2x2x2 supercell. Displayed is the change in free formation energy regarding the change of the k-mesh or k-grid.

KPOINTS – Convergence

K_Points	Free Formation Energy [eV]
2x2x2	-177.4491
4x4x4	-177.4891
6x6x6	-177.4544
8x8x8	-177.4994
10x10x10	-177.4994

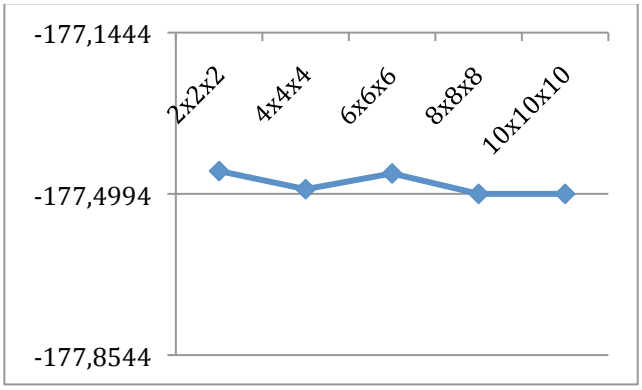

Table-A 5: Free formation energy convergence relative to the Cut Off energy of a 2x2x2 super cell. Displayed is the change in free formation energy regarding the change of the energy cut off or r_c

ECUT – Convergence

ECUT	Free Formation Energy [eV]
350	-177.5924
400	-177.5307
450	-177.5212
500	-177.531
550	-177.5011
600	-177.4838

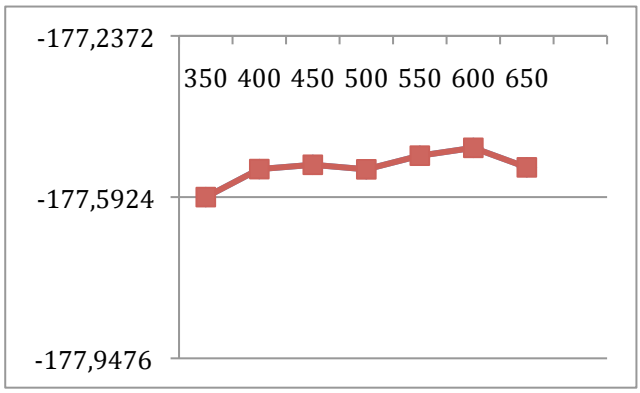

The data provided by table-A 6 was used to calculate the free formation energy and the point defect formation energy for this thesis. Therefore the data should be available for further investigations of similar problems as well as for comparison studies.

Table-A 6: Free formation energies of pure systems in various super cell configurations and the free energy formation for one atom.

Free Formation Energy (E_F) of the pure Components

Elements	E_F [eV]	E_F for each atom [eV]
Ni	-176.4502	-5.5141
Al	-119.7507	-3.7422
C	-3.5443	-1.7722
Cl	-16.6287	-8.3144
N	-9.8784	-4.9392
O	-122.7560	-3.8361
S	-176.8972	-5.5280

Graph-A 1 is obtained through simulation results of point defect formation energies for a pure Ni 2x2x2 super cell.

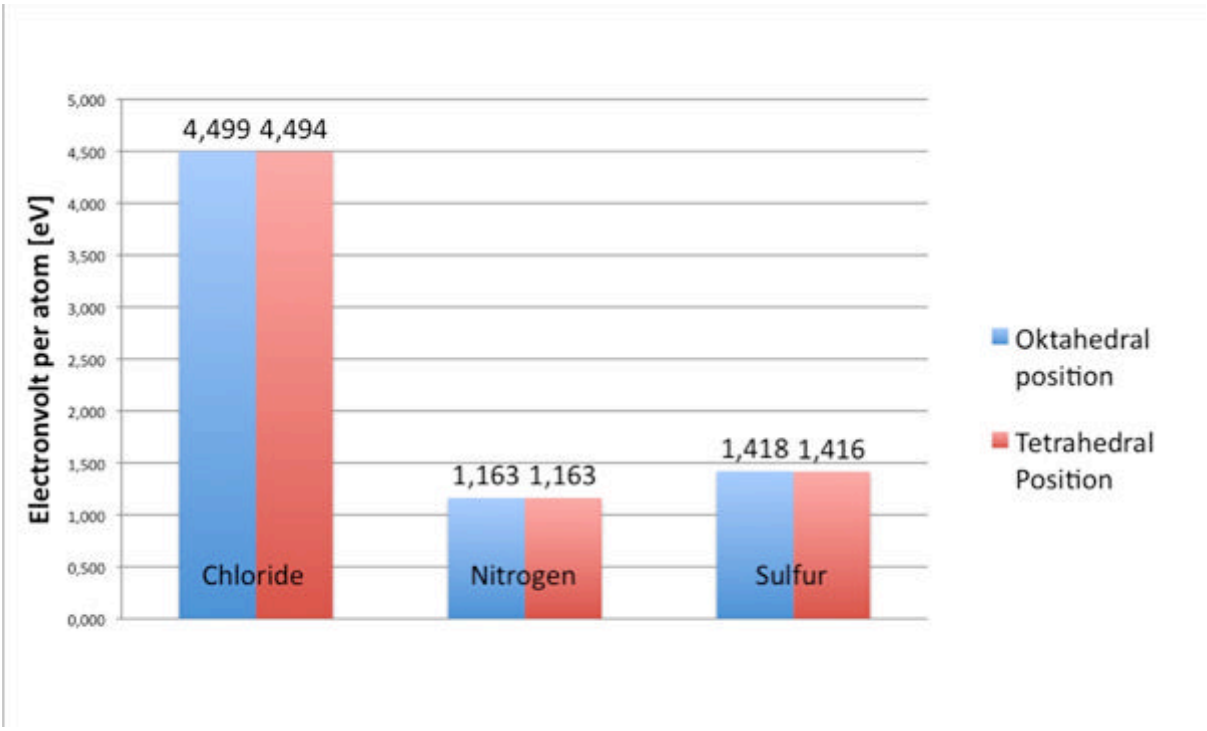

Graph-A 1: Displayed is the point defect energy for a pure 2x2x2 nickel super cell with 3 different interstitial atoms at 2 different site locations. Clearly chloride needs a large amount of energy to be introduced into the system, while Nitrogen and sulfur only need ~ ¼ of the energy necessary.

Compared to previous simulation results, it is noteworthy that the elements displayed above need energy in order to be introduced as a single point defect into the system. Carbon and oxygen lead to a more stable system, while chloride, nitrogen and sulfur are destabilizing the system.

Graph-A 2 provides further data for the behavior of interstitial elements in connection with the increasing aluminum content in the material.

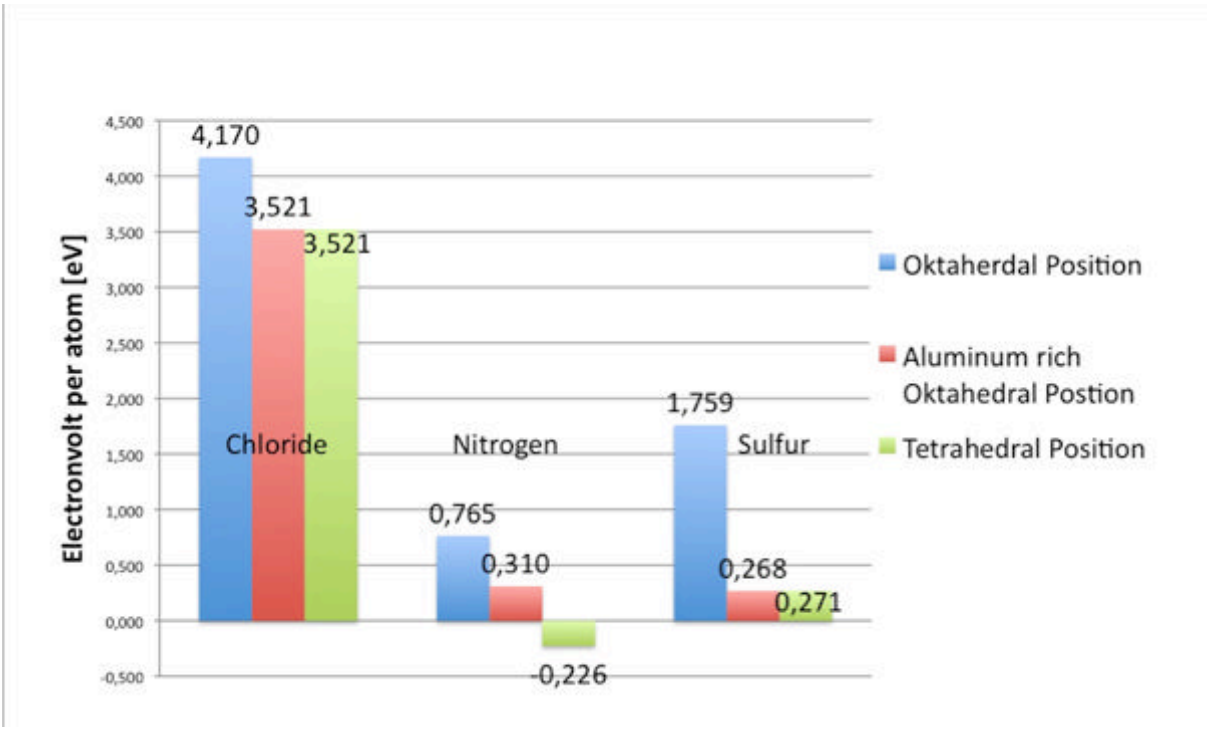

Graph-A 2: Displayed is the point defect formation energy for a 2x2x2 Ni_3Al super cell. The aluminum rich site position is preferred by all elements introduced into the system, but only nitrogen is able to create a stable energy formation. Consequently, it is most likely to be located at the very same position.

It is obvious that the interstitial elements prefer to be close to aluminum (nitrogen in particular), indicated by the aluminum-rich tetrahedral position. The point defect energies calculated are closer to the results obtained with the 3x3x3 super cell simulations. Therefore, there is a high chance to have a similar experimental result.

The interstitial elements are going to avoid nickel–rich and rather go for the aluminum rich phases in the material. Although the influence of wide and low angle grain boundaries as well as coherent interfaces is not considered in the simulation results, there is a chance of the elements behaving as calculated in an environment closely related to a bulk system.